

# Evaluation of Flow Solver Accuracy using Five Simple Unsteady Validation Cases

Bradford E. Green, Ryan Czerwiec  
*Naval Air Systems Command, Patuxent River, MD, 20670*

Chris Cureton, Chad Lillian, Sergey Kernazhitskiy, Tim Eymann, Jason Torres  
*Air Force SEEK Eagle Office, Eglin Air Force Base, FL, 32542*

Keith Bergeron, Robert Decker  
*United States Air Force Academy, USAF Academy, CO, 80840*

The goal of this study was to evaluate the time accuracy of five different Navier-Stokes flow solvers using five simple two-dimensional validation cases. The five flow solvers included Cobalt, USM3D, FUN3D, Beggar and NASCART-GT. The five validation cases included the laminar flow over a circular cylinder, the laminar shock tube, the inviscid convecting vortex, the 18%-thick circular-arc airfoil and the NACA 0015 pitching airfoil. This study was conducted in an effort to better understand the capabilities of each flow solver for time-accurate calculations. The eventual goal of the project was to use one or more of these flow solvers to analyze the unsteady transonic flow over a fighter aircraft with stores in captive carriage. Evaluating the capabilities of each flow solver with simple validation cases rather than a complicated fighter aircraft was desirable.

## Nomenclature

$a$	=	speed of sound
$c$	=	chord of airfoil
$c_a$	=	2D axial force coefficient
$c_d$	=	2D drag coefficient
$c_l$	=	2D lift coefficient
$c_m$	=	2D pitching-moment coefficient
$c_n$	=	2D normal force coefficient
$Ch$	=	wall heat coefficient
$e$	=	internal energy
$f$	=	frequency
$k$	=	reduced frequency
$L$	=	reference length
$M$	=	Mach number
$p$	=	static pressure
$Re$	=	Reynolds number
$St$	=	Strouhal number
$T$	=	static temperature
$t$	=	time
$u$	=	velocity
$x$	=	x dimension
$y$	=	y dimension
$z$	=	z dimension
$\alpha$	=	angle of attack (degrees)
$\phi$	=	pitch angle (degrees)
$\Gamma$	=	vortex strength
$\rho$	=	density
$\tau$	=	thickness

$\omega$  = vorticity  
 $\infty$  = freestream

## I. Introduction

With recent advances in computers and turbulence models, computational fluid dynamics (CFD) is being used more than ever before to compute the complicated flow over military aircraft. The advances in computers allow for larger grids to be generated and the final CFD solutions to be obtained faster. Steady-state solutions at a single condition on unstructured grids with approximately 50 million cells can be obtained in 12 hours or less. Complete polars with 15 angles of attack can be completed in a few days. Depending on the availability of computers, sometimes these polars can be obtained in only one day. The computer times for structured flow solvers and grids are even less.

The above estimates are for steady-state solutions. Sometimes, though, unsteady calculations must be performed to obtain accurate results. These time-accurate calculations add to the complexity of the problem, since the time step and number of Newton subiterations must be chosen properly to generate an accurate solution. Therefore, when doing time-accurate calculations, it is important to understand the impact that time step and Newton subiterations have on the flow solution.

Despite the ability to generate larger grids and use improved turbulence models, caution must still be taken when generating flow solutions. Flow solver, grid, turbulence model, time step and Newton subiteration studies should still be conducted. In addition, the results should be compared to known wind-tunnel or flight-test data where possible to ensure that accurate solutions are being generated.

The eventual goal of this work is to predict the unsteady flow over a fighter aircraft with stores in captive carriage. Before embarking on this challenging problem, it was desired to validate the CFD tools with several simple two-dimensional validation cases. CFD could only be expected to generate accurate data on the unsteady, three-dimensional fighter-aircraft problem if CFD were first able to accurately predict some basic validation cases.

Five unsteady validation cases were selected for this study. These cases include the laminar flow over a circular cylinder, the laminar shock tube, the inviscid convecting vortex, the 18%-thick circular-arc airfoil and the NACA 0015 pitching airfoil. The goal of this work was to analyze these five validation cases with five different flow solvers. These flow solvers include Cobalt, USM3D, FUN3D, Beggar and NASCART-GT. While the developers of all flow solvers use a basic set of validation cases to prove the accuracy of the particular flow solver, these validation cases often vary from one flow solver to another. While these validation cases may be similar between different flow solvers, they are not always identical. In this study, each of the flow solvers will be run on the same set of validation cases allowing for the results to be compared.

The flow solvers will be introduced in the following section. The results of the validation cases will then be presented, followed by a brief summary.

## II. Flow Solvers

### A. Cobalt

The commercial flow solver Cobalt [1] is a Navier-Stokes flow solver that solves the Navier-Stokes equations using a cell-centered, finite-volume approach applicable to arbitrary cell topologies. Since Cobalt accepts arbitrary cell topologies and can be used on both two- and three-dimensional grids, it will be possible to use Cobalt to analyze any of the grids that are generated during this project. Cobalt is second-order accurate in space and time. A Newton sub-iteration scheme is employed for time-accurate calculations. Several different turbulence models have been coded in Cobalt, including Spalart-Allmaras (SA) [2], SA with rotation correction, Wilcox  $k-\omega$  and Menter's shear stress transport (SST) [3] model. The SA and SST turbulence models can be combined with the Delayed Detached-Eddy Simulation (DDES) for time-accurate calculations. Cobalt is also capable of analyzing overset grids and cases employing rigid body motion.

### B. USM3D

USM3D [4], which was developed at NASA Langley Research Center and is part of the Tetrahedral Unstructured Software System (TetrUSS), is a three-dimensional, cell-centered, finite-volume Navier-Stokes flow solver for unstructured, tetrahedral meshes. USM3D uses Roe's flux-difference splitting technique to compute the inviscid flux quantities across each cell face. The MinMod flux limiter is also implemented within USM3D. The implicit Gauss-Seidel time-stepping scheme is used to advance the solution to a steady-state condition. USM3D is

second-order in space and time. The one-equation SA turbulence model and the two-equation Mentor's SST model are available within USM3D. Spalart-Allmaras is used to form a Detached-Eddy Simulation (DES) model for time-accurate calculations. It is important to mention that the DDES model available in Cobalt is a variation of the DES model available in USM3D.

### C. FUN3D

The FUN3D [5] flow solver was developed at NASA Langley Research Center. FUN3D solves the Navier-Stokes equations on unstructured two- and three-dimensional grids. The flow solver is node-based and uses a finite-volume discretization. FUN3D employs multigrid with implicit time stepping where the linear system is solved using either point-implicit, line-implicit or Newton-Krylov schemes. The FUN3D options for upwind flux functions include Roe flux-difference splitting, Van Leer flux-vector splitting, AUFS and HLLC. The SA and SST turbulence models are also available within FUN3D. The time-accurate calculations within FUN3D are third-order accurate with error controllers. FUN3D is also capable of analyzing problems with time-varying translation and rotation.

### D. Beggar

The Beggar code [6], which originated at the Wright Laboratory, is currently being maintained and developed at the Air Force Seek Eagle Office (AFSEO) at Eglin Air Force Base in Fort Walton Beach, FL. Beggar is a computational tool that can predict the flow over stores as they separate from aircraft and can calculate the trajectories and orientations of the stores as they separate. As a result, grid assembly, flow solver and six degree-of-freedom (DOF) components exist within Beggar. For this project, only the capabilities of Beggar as a flow solver will be evaluated.

Beggar solves the Euler and Navier-Stokes equations on blocked and overset structured grids. Beggar solves the governing equations using a finite-volume, cell-centered discretization. The Steger-Warming scheme or the Roe scheme can be used to calculate the inviscid fluxes. The Baldwin-Lomax [7], SA and k-epsilon turbulence models are used by Beggar for turbulent flows. Beggar can be used in both steady-state and time-accurate modes. DES is also available for use with SA for time-accurate calculations.

### E. NASCART-GT

NASCART-GT, which was developed at Georgia Tech, is capable of solving the Euler equations, the Euler equations with an integral boundary layer and the Navier-Stokes equations on two- and three-dimensional Cartesian grids. NASCART-GT uses adaptive mesh refinement in high flow gradient regions to improve the accuracy and efficiency of the solution. Before solving the governing equations, NASCART-GT generates a Cartesian grid on the specified geometry in an automated fashion, reducing the grid generation time usually required before a flow solver can be executed. NASCART-GT is up to fifth-order accurate in space and uses Roe's Approximate Riemann solver, AUSM and AUSMPW+ schemes. NASCART-GT is up to second-order accurate in time. The k-epsilon turbulence model is available within NASCART-GT.

## III. Summary of Validation Cases

The goal of this work was to use five validation cases to evaluate the accuracy of each of the five flow solvers. These cases include the laminar flow over a circular cylinder, the laminar shock tube, the inviscid convecting vortex, the NACA 0015 pitching airfoil, and the 18%-thick circular-arc airfoil. All of these cases are viscous, with the exception of the inviscid convecting vortex case. The NACA 0015 pitching airfoil and the 18%-thick circular-arc airfoil are turbulent cases while the circular cylinder and shock tube cases are laminar cases.

Table 1 summarizes the flow conditions, reference length and time-steps that were used with Cobalt for each validation case. In this table, the Reynolds number is based on the reference length shown in the table. For some of these cases, the free-stream temperature and pressure are arbitrary, but the Reynolds number shown in the table must be maintained with each flow solver.

The flow conditions and reference length for the shock tube and convecting vortex cases are shown in metric units in Table 1. These cases can also be evaluated in English units. In doing so, the grid remains the same and the reference length becomes 1 ft. The pressure and temperature must be set to give the correct value for Reynolds number.

The time steps given in Table 1 are non-dimensional. The dimensional time steps can be calculated using the equation:

$$\Delta \bar{t} = \Delta t \frac{L}{a_\infty}$$

**Table 1. Summary of flow conditions for validation cases.**

Validation Case	Mach	Re <sup>+</sup>	$\alpha$	T <sub>∞</sub> <sup>+</sup>	P <sub>∞</sub> <sup>+</sup>	L	Δt
Circular cylinder	0.2	150	0°	500 R	0.21377 psf	1 ft	0.025 0.1
Shock tube	0.5	50,000	0°	288.15 K	869.8 Pa	1 m	0.000625 0.00125 0.0025
Convecting vortex	0.5	N/A	0°	398.208 K	101,325 Pa	1 m	0.04
Pitching airfoil	0.29	1.95x10 <sup>6</sup>	Prescribed	500 R	1897.576 psf	1 ft	0.10703 0.21406
Circular-arc airfoil	0.76	12x10 <sup>6</sup>	0°	500 R	4478.97 psf	1 ft	0.001644 0.003288 0.006576 0.01315 0.0263 0.0526
* Reynolds number is based on the reference length L							
+ Pressure and temperature are arbitrary, but the Reynolds number must be maintained							

In the following sections, each of the validation cases will be discussed. Each of these sections contains a description of the validation case, a description of the computational grids that were used and a summary of results.

#### IV. Laminar Flow over Circular Cylinder

##### A. Description

The laminar flow over a circular cylinder was used to evaluate the ability of each flow solver to predict a periodic unsteady viscous flow. For this problem, the laminar Navier-Stokes equations were solved. The flow conditions for this validation case were taken from Nichols et al. [9] and are shown in Table 1. Two different time steps were used for the calculations. The number of Newton sub-iterations was varied to ensure temporal accuracy. The Strouhal number and amplitude of the cylinder lift and drag coefficients were evaluated as well as the average value of the drag coefficient. These same quantities were evaluated by Nichols. The Strouhal number is defined as

$$St = \frac{f\tau}{u_\infty}$$

##### B. Computational Grids

For the circular cylinder validation case, each flow solver analyzed one grid. For Cobalt and BEGGAR, the structured grid of Nichols was used. This grid is shown in Figure 1. This grid had 401 points on the cylinder and 201 points normal to the cylinder. The normal spacing at the surface of the cylinder was 0.001043 diameters. The farfield boundary was placed 98.7 diameters from the surface of the cylinder. For USM3D and FUN3D, an unstructured tetrahedral grid of similar grid spacing was generated. This grid is shown in Figure 2.

##### C. Results

The results for the circular cylinder validation case are shown in Figures 3 through 9. In Figure 3, the lift coefficient from the Cobalt flow solver is plotted versus time over one cycle of the flow. On this plot, arrows illustrate the value of the lift coefficient at nine different times along this cycle. The times are labeled with letters A through I. In Figure 4, the Mach contours in the vicinity of the cylinder are shown at the times labeled in Figure 3.

Using Figure 4, one is able to visualize how the flow is changing with time. The Mach contours illustrate the shedding of vorticity from the cylinder.

In Figure 5, the lift amplitude is plotted as a function of the number of sub-iterations for the small and large time steps for Cobalt, USM3D, FUN3D and Beggar. This plot confirms that the lift amplitude converges for both time steps as the number of sub-iterations is increased. The converged values of lift amplitude vary between 0.73 and 1.09. The lift amplitude is a measure of how damped the solutions are for each of the flow solvers.

In Figure 6, the lift Strouhal number is plotted for each of the flow solvers. This figure shows that the lift Strouhal number converges for each of the flow solvers as the number of sub-iterations is increased. Based on the available experimental data, the lift Strouhal number should be approximately 0.179 to 0.182 [9, 10 and 11]. The lift Strouhal number for each of the flow solvers was in the vicinity of the experimental data.

In Figure 7, the average drag value is plotted for each of the flow solvers. Once again, the average drag value converges as the number of sub-iterations is increased. The values for the converged average drag coefficient predicted by the flow solvers range from 1.29 to 1.38. Based on experimental data, the average drag coefficient should be approximately 1.34 [9].

In Figure 8, the drag amplitude is plotted for each of the flow solvers. In these plots, the converged drag amplitude varies between 0.0269 and 0.059. As in the case of the lift amplitude, the drag amplitude is a measure of how damped the solutions are.

In Figure 9, the drag Strouhal number is plotted for each of the flow solvers. Once again, the drag Strouhal number converges as the number of sub-iterations is increased. The values of drag Strouhal number in the plot range from 0.34 to approximately 0.37.

Attempts to run the NASCART-GT flow solver on this validation case were not successful.

## V. Inviscid Convecting Vortex

### A. Description

The inviscid convecting vortex validation case was also used to evaluate each of the flow solvers. For this case, the Euler (inviscid) equations were solved. This validation case presented the opportunity to evaluate the ability of the flow solvers to maintain the shape and strength of a vortex while it is convected downstream. The ability of a flow solver to convect a vortex downstream when analyzing a complex military aircraft is very important. In flight, vortices from the wing on an aircraft can impact the flow over horizontal tails. If the vortex is not properly convected downstream in the CFD simulation, then the resulting forces and moments on the tail will be inaccurate.

The boundary conditions for this problem were taken from Nichols [8]. The initial vortex strength was prescribed as:

$$\omega = \frac{\Gamma}{2\pi} (2 - \bar{R}) \exp(0.5(1 - \bar{R}))$$

where

$$\bar{R} = (x - x_0)^2 + (z - z_0)^2,$$

$x_0$  and  $z_0$  represent the location of the vortex center. A vortex strength of 5 was chosen for this study.

Rather than initializing the flow solution with the traditional free-stream values at the beginning of the CFD calculation, each flow solver had to be modified to prescribe the vortex described above. This task alone was very challenging. In several cases, the vortex was not prescribed properly and erroneous results were generated. Caution must be taken when prescribing the initial vortex. In the case of the commercial flow solver Cobalt, the developers of the code made the modifications to the code since the source code is not distributed to the users of the software.

The flow conditions used within Cobalt for this problem are shown in Table 1. The vortex was allowed to complete 5 cycles (500 time steps/cycle). The minimum pressure of the vortex was tracked to examine the ability of the flow solvers to maintain the vortex strength.

### B. Computational Grids

For the inviscid convecting vortex validation case, three structured grids were used as the baseline grids. These grids were those of Nichols. These grids were 10 units in height by 10 units in width. The number of points in each of these grids was varied in an effort to determine the impact of grid spacing on the convecting vortex. The coarse

grid was 41 x 41, which corresponds to a grid spacing of 0.25 units. The medium grid was 81 x 81, which corresponds to a grid spacing of 0.125 units. The fine grid was 161 x 161, which corresponds to a grid spacing of 0.0625 units. These structured grids are shown in Figure 10.

To generate the solutions with Cobalt, the baseline set of structured grids were used. The vortex was placed in the center of the grid. Through the use of a periodic boundary condition, the vortex was progressed five cycles on each grid.

Unfortunately, none of the other flow solvers used were capable of using a periodic boundary condition. For the Beggar flow solver, the baseline set of grids (those shown in Figure 10) were modified to eliminate the need for a periodic boundary condition. Each of the grids were modified by extrapolating the grids to the right (in the positive x-direction) while maintaining the grid spacing. The extrapolated grids had a height of 10 units and a width of 50 units. Unstructured tetrahedral grids with the same dimensions and similar grid spacings were generated for use with USM3D and FUN3D. The coarse, medium and fine unstructured grids are shown in Figure 11.

### C. Results

In Figures 12 through 14, the results of the Cobalt, Beggar and FUN3D flow solvers are shown. In these figures, the contours of the vortex after five cycles for the coarse, medium and fine grids are compared to the contours of the initial vortex. The impact of grid spacing on the vortex is obvious. For the fine grid, the contours of the vortex are nearly maintained after five cycles with each flow solver. As the grid becomes more coarse, the contours of the vortex are not maintained. For the ideal flow solver and grid, the contours of the initial vortex would be maintained.

In Figure 15, the results of the USM3D flow solver are shown for the fine grid after five cycles of the vortex. The contours of the vortex are maintained on the fine grid. Plots of the medium and coarse grids were not available.

In Figure 16, the minimum pressure as a function of the number of vortex cycles and grid size is shown for Cobalt, USM3D, FUN3D and Beggar. The results are consistent across all four flow solvers. Fine grids are better able to convect the vortex than coarse grids.

The minimum pressure is plotted in Figure 17 for the NASCART-GT flow solver. In this case, the initial minimum pressure is not maintained, even for the fine grid. A lot of effort was expended to find the source of this problem, which also plagued several of the other flow solvers during the course of this validation case. The problem for all of the flow solvers was traced to an incorrect initialization of the vortex within the flow solver. The other flow solvers were corrected and meaningful results were generated. However, due to time and budget limitations, the NASCART-GT was dropped from the project at this point.

## VI. Laminar Shock Tube

### A. Description

A laminar shock tube problem was used to evaluate the ability of each flow solver to properly calculate the shock motion as a function of time. For this problem, the laminar Navier-Stokes equations were solved. Including the viscous effects presented the opportunity to calculate the heat transfer characteristics for this problem. The initial conditions for this problem were taken from Nichols [8] and are shown in Table 2.

**Table 2. Initial conditions for shock tube validation case.**

	$\rho/\rho_{ref}$	$p/p_{ref}$	$T_{wall}/T_{ref}$
Left state	1.0	1.0	1.0
Right state	0.1	0.1	1.0

The flow conditions for this problem are shown in Table 1. The free-stream values from Table 1 were used for the reference conditions shown in Table 2. Isothermal, no-slip boundary conditions were used on the upper and lower walls and a temperature of 288.15 degrees Kelvin was specified on the two walls.

The density, pressure, velocity and internal energy on the centerline of the shock tube and the wall heat transfer coefficient were calculated at a non-dimensional time of 0.2. The density, pressure, velocity and internal energy were compared to the inviscid theoretical results and the wall heat transfer coefficient was compared with the results of Nichols.

### B. Computational Grids

The structured grid used for the shock tube validation case was that of Nichols. This structured grid, which is shown in Figure 18, was used by Cobalt and Beggar. For FUN3D and USM3D, unstructured tetrahedral grids were

generated. These grids are shown in Figure 19. Each grid was 1 unit in width and 0.1 units in height. The upper and lower walls were viscous with a normal spacing of approximately 0.0001 units.

### C. Results

The results for the laminar shock tube problem are presented in Figures 20 through 24. All of the results in these figures show the state of the solution at a non-dimensional time of 0.2. Where applicable, the results are compared to the exact solution. The results from all three time steps are shown in the plots.

In Figure 20, the density is plotted as a function of  $x$  for the Cobalt, USM3D, FUN3D and Beggar flow solvers. The FUN3D results tend to overshoot the exact solution. This is probably a result of the fact that FUN3D is a node-based solver. A finer grid might yield a better correlation with the exact solution.

In Figures 21, 22 and 23, the pressure, velocity and internal energy are plotted as a function of  $x$ . The same overshoot with FUN3D is present in each of the figures.

In Figure 24, the wall heat transfer coefficient is plotted as a function of  $x$  for Cobalt. The other flow solvers were unable to output the wall heat transfer coefficient. The Cobalt results for wall heat transfer coefficient are compared to those of Nichols, which are also included in the plot.

The Beggar flow solver was not used for the remaining validation cases in this paper. Time and budget issues dictated that it be dropped from the suite of flow solvers being used during this project.

## VII. 18%-Thick Circular-Arc Airfoil

### A. Description

The 18%-thick circular-arc airfoil (also known as the bi-convex airfoil) was used to evaluate the flow solvers. For this problem, the turbulent Navier-Stokes equations were solved. The SA and SST turbulence models were evaluated for each flow solver. The CFD results were compared to wind-tunnel data obtained by McDevitt [12]. Shock-induced boundary-layer separation and a hysteresis effect are present in the transonic flow over the bi-convex airfoil. The goal of this validation exercise was to determine if each of the flow solvers could predict these phenomena. The axial force, normal force and pitching-moment coefficients, as well as the reduced frequency, were evaluated during these calculations. As shown in Table 1, the majority of these calculations were performed at Mach 0.76. The approach of Rumsey et al. [13] was used during the current study.

### B. Computational Grids

The two-dimensional structured grid of Rumsey was used by Cobalt for the 18%-thick circular-arc airfoil validation case. This grid is shown in Figure 25. The C-type grid has 257 points around the airfoil and 81 points normal to the airfoil. The grid had 177 points on the airfoil itself. The grid extends 20 chord lengths in each direction to the farfield. The viscous spacing normal to the airfoil is approximately 0.000004 chord lengths. Unstructured tetrahedral grids of similar size and grid spacing were generated for FUN3D and USM3D. This unstructured grid is shown in Figure 26.

### C. Results

The results for the 18%-thick circular-arc airfoil validation case are presented in Figures 27 through 35. In Figure 27, the normal force coefficient as a function of time is plotted for one cycle of the flow at Mach 0.76. The Cobalt flow solver with the SST turbulence model was used to generate these results. In this plot, nine instances in time are labeled with the letters A through I. In Figure 28, contours of Mach number are shown in the vicinity of the 18%-thick circular-arc airfoil for the times labeled in Figure 27. This figure shows the unsteadiness of the flow, which results from the shock-induced flow separation which occurs on the airfoil. It is important to point out that the airfoil was stationary during these calculations. The unsteadiness that is seen in the figure is not due to any motion of the airfoil. The snapshots in Figure 28 show that the flow separation on the airfoil oscillates between the upper and lower surfaces.

The results in Figures 29 and 30 are for static cases ran at Mach 0.76. These plots show the impact of time step, sub-iterations and turbulence model on the reduced frequency, which is defined as

$$k = \frac{2\pi f(0.5c)}{u_\infty}$$

When calculating the reduced frequency, the pressure component of the lift coefficient is used.

In Figure 29, the reduced frequency is plotted as a function of time step for the Cobalt, FUN3D and USM3D flow solvers and the SA and SST turbulence models. In general, the reduced frequency converges as the time step is reduced. Converged values of the reduced frequency range from 0.47 to 0.51. Based on experimental data, the reduced frequency is 0.49.

In Figure 30, the reduced frequency is plotted as a function of the number of sub-iterations. The reduced frequency for Cobalt is converged after 10 sub-iterations. The reduced frequency for USM3D and FUN3D do not appear to be converged after 20 sub-iterations. Once again, based on experimental data the reduced frequency is 0.49.

In the second phase of this study, the ability of the flow solvers to predict the hysteresis effect was evaluated. To do this, an initial time-accurate solution was obtained at Mach 0.7. Once converged, the airfoil was analyzed at Mach 0.71 starting from the final solution of the Mach 0.7 calculations. Once converged, the Mach 0.72 calculations were started using the final solution of the Mach 0.71 case. This process was continued for Mach 0.73, 0.74, 0.75 and 0.76. Once the Mach 0.76 calculations were converged, the Mach number was reduced to Mach 0.7 at 0.01 increments. Each case at a new Mach number restarted from the solution at the previous Mach number. Time-accurate solutions were generated for each Mach number.

The results for the hysteresis calculations are shown in Figures 31 through 33. In these figures, the axial-force, normal-force and pitching-moment coefficients are plotted as a function of time and Mach number for Cobalt, USM3D and FUN3D. The results for both the SA and SST turbulence models are shown in the plots. For increasing Mach number, Cobalt, FUN3D and USM3D predict the onset of unsteadiness between Mach 0.73 and Mach 0.74. For decreasing Mach number, Cobalt and FUN3D predict the onset of steadiness between Mach 0.73 and Mach 0.72 while USM3D predicts the onset of steadiness between Mach 0.74 and Mach 0.73. For USM3D, the change between steady flow and unsteady flow is between Mach 0.73 and Mach 0.74 regardless of whether the Mach number is increasing or decreasing.

In Figure 34, the results for USM3D at Mach 0.735 are shown. At this Mach number, the flow is steady if the Mach number is increasing (as shown in the left plot of Figure 34) and unsteady if the Mach number is decreasing (as shown in the right plot of Figure 34). Therefore, USM3D predicts the hysteresis effect, but at a slightly different Mach number than Cobalt and FUN3D. For Cobalt and FUN3D, the flow is steady at Mach 0.73 if the Mach number is increasing and unsteady at Mach 0.73 if the Mach number is decreasing. During a wind-tunnel experiment of this airfoil, unsteady flow began at Mach 0.76 for increasing Mach number and unsteady flow ceased at Mach 0.73 for decreasing Mach number. [14]

In Figure 35, the free-stream Mach numbers where regions of unsteady flow were predicted by CFD are plotted for increasing and decreasing Mach number. These results are compared with the unsteady regions seen during the WT test. When analyzing this figure, it is important to note that CFD results were generated between Mach 0.7 and Mach 0.76. No CFD results were generated above Mach 0.76. However, WT data was produced above Mach 0.76. For increasing Mach number, CFD predicts the onset of unsteady flow at a lower Mach number than was seen in the WT test. For CFD, the onset of unsteady flow begins at Mach 0.74. For the WT test, the onset begins at Mach 0.76. The reason for this difference between CFD and WT is unknown.

For decreasing Mach number, unsteady flow is predicted by CFD to Mach 0.73 or Mach 0.735, depending on the flow solver. Unsteady flow continues during the WT test to Mach 0.73. There is general agreement between CFD and the WT test in this regard.

## VIII. NACA 0015 Pitching Airfoil

### A. Description

The low angle of attack pitching NACA 0015 airfoil case of Piziali [15] was also included as a validation case for this project. For this case, the turbulent Navier-Stokes equations were solved. The SA and SST turbulence models were evaluated. This case provided the opportunity to validate each of the CFD codes for a simple rigid body motion. For the angle of attack range being studied here, the flow is attached throughout the majority of the cycle. This allows some of the flow solvers being used during this project to be run in 2-D mode. The flow conditions for this case are shown in Table 1. The angle of attack was prescribed as

$$\alpha = 4^\circ + 4.2^\circ \sin(2\pi ft)$$

where  $f$  is the frequency of oscillation. A frequency of oscillation of 10 cycles per second was used for the calculations. The airfoil is rotated about the quarter-chord point.

## B. Computational Grids

The structured grid of Nichols was used by the Cobalt flow solver. This grid is shown in Figure 36. This is a C-type grid with 441 points around the surface and 71 points normal to the surface. The grid had 241 points on the airfoil itself. The grid spacing at the surface in the normal direction is 0.00001 chord lengths. The farfield boundaries of the grid are approximately 25 chord lengths from the airfoil surface. An unstructured tetrahedral grid was generated for use with the USM3D and FUN3D flow solvers. This grid is shown in Figure 37.

## C. Results

In Figure 38, contours of Mach number are shown in the vicinity of the airfoil as the airfoil is pitched from  $4^\circ$  to  $8.2^\circ$  to  $-0.2^\circ$  to  $4^\circ$ . The results of the Cobalt flow solver and the SST turbulence model were used for this figure. The acceleration of the flow around the leading edge at the higher pitch angles is clearly evident in the Mach contours. The Mach contours also indicate that the flow is attached throughout the majority of the pitch cycle.

The lift, drag and pitching-moment coefficients are plotted as a function of pitch angle in Figures 39, 40 and 41. The results for the wind tunnel data and the Cobalt, FUN3D and USM3D flow solvers are included. Each flow solver was run with both the SA and SST turbulence models. In each case, only the pressure component of the forces and moments are being compared.

In Figure 39, the lift coefficient is plotted. The Cobalt results compare well to the WT data. The FUN3D results compare well to the WT data at the lower pitch angles. At the higher pitch angles, FUN3D does not predict the hysteresis effect as the results for the up-sweep and down-sweep are nearly identical. The hysteresis effect is predicted with USM3D, but the results under-predict the lift at the higher pitch angles. The differences between the SA and SST results are not significant.

The drag coefficient is plotted in Figure 40. Each flow solver accurately predicts the shape of the data. Cobalt and USM3D appear to under-predict the drag, while FUN3D over-predicts the drag. Once again, the differences between the SA and SST models are subtle.

In Figure 41, the pitching-moment coefficient is plotted as a function of pitch angle. Each flow solver is able to predict the shape of the plot. While Cobalt appears to be closest to the WT data, the results of each flow solver are “rotated” from the WT data. It’s interesting to note that the FUN3D/SST results predict the “roughness” of the data. The curves from the other plots are smooth.

## IX. Summary

The goal of this study was to evaluate the time accuracy of five different Navier-Stokes flow solvers using five simple two-dimensional validation cases. The five flow solvers included Cobalt, USM3D, FUN3D, Beggar and NASCART-GT. The five validation cases included the laminar flow over a circular cylinder, the laminar shock tube, the inviscid convecting vortex, the 18%-thick circular-arc airfoil and the NACA 0015 pitching airfoil. This study was conducted in an effort to better understand the capabilities of each flow solver for time-accurate calculations. The eventual goal of the project was to use one or more of these flow solvers to analyze the unsteady transonic flow over a fighter aircraft with stores in captive carriage. Evaluating the capabilities of each flow solver with simple validation cases rather than a complicated fighter aircraft was desirable.

While the goal of the project was to evaluate all five flow solvers on all five validation cases, the NASCART-GT flow solver was not successfully validated on any of the validation cases. The remaining four flow solvers were successfully used on the circular cylinder, laminar shock tube and inviscid convecting vortex validation cases. The Cobalt, USM3D and FUN3D flow solvers were successfully used on the 18%-thick circular-arc airfoil and the NACA 0015 pitching airfoil validation cases. Funding, time and flow solver limitations were the main reasons that all five flow solvers were not successfully used on all five validation cases.

For the calculations that were completed, the CFD results compare well to the validation data that was provided. There are cases, however, where the CFD results do not compare well to the data. An example of this can be seen in the results of the pitching-moment coefficient for the NACA 0015 pitching airfoil. Since the Cobalt, FUN3D and USM3D flow solvers were successfully used on all five validation cases, these three flow solvers would be the best choices for accurately predicting the transonic, unsteady flow over a fighter aircraft with stores in captive carriage. This conclusion is based on the results of this study alone. Evaluating the abilities of these flow solvers to accurately predict the flow over the fighter aircraft alone and the stores/weapons alone would provide more information on making a decision regarding the flow solver or solvers that could accurately predict the complex problem at hand.

## Acknowledgments

The authors would like to thank the Institute for HPC (High Performance Computing) Applications to Air Armament (IHAAA) program for funding this project. The computer time used for the CFD calculations during this project was obtained from the HPC Modernization Program (HPCMP). The authors would like to acknowledge Mr. B.L. Chesser, AFSEO, and Dr. Robert Nichols, UAB, for their help and guidance during this project.

## References

- [1] Strang, W. Z., Tomaro, R. F., and Grismer, M. J., "The Defining Methods of Cobalt60: a Parallel, Implicit, Unstructured Euler/Navier-Stokes Flow Solver," AIAA-1999-0786, January 1997.
- [2] Spalart P., and Allmaras S. A., "One-Equation Turbulence Model for Aerodynamic Flows," AIAA-1992-0439, January 1992.
- [3] Menter, F.R., "Improved Two-Equation k-omega Turbulence Models for Aerodynamic Flows", NASA TM-103975, October 1992.
- [4] Frink, N. T., "Tetrahedral Unstructured Navier-Stokes Method for Turbulent Flows," *AIAA Journal*, Vol. 36, No. 11, Nov. 1998, pp. 1975-1982.
- [5] Anderson, W. K., Rausch, R. D., and Bonhaus, D. L., "Implicit/Multigrid Algorithms for Incompressible Turbulent Flows on Unstructured Grids," *Journal of Computational Physics*, Vol. 128, Issue 2, 1996, pp. 391-408.
- [6] Rizk, M., Ellison, S., Prewitt, N., "Beggar – A Store Separation Predictive Tool", AIAA-2002-3190, June 2002.
- [7] Baldwin, B. S., and Lomax, H., "Thin Layer Approximation and Algebraic Model Separated Turbulent Flows," AIAA-1978-257, January 1978.
- [8] Nichols, R. H., and Heikkinen, B. D., "Validation of Implicit Algorithms for Unsteady Flows Including Moving and Deforming Grids," AIAA-2005-0683, January 2005.
- [9] Tritton, D. J., "Experiments on the Flow Past a Circular Cylinder at Low Reynolds Numbers," *Journal of Fluid Mechanics*, Vol. 6, 1959, pp 547-567.
- [10] Roshko, A., "On the Development of Turbulent Wakes from Vortex Streets," NACA Report 1191, 1954.
- [11] Friehe, C. A., "Vortex Shedding from Cylinders at Low Reynolds Numbers," *Journal of Fluid Mechanics*, Vol. 100, Part 2, 1980, pp. 237-241.
- [12] McDevitt, J. B., "Supercritical Flow about a Thick Circular-Arc Airfoil," NASA TM 78549, January 1979.
- [13] Rumsey, C. L., Sanetrik, M. D., Biedron, R. T., Melson, N. D., and Parlette, E. B., "Efficiency and Accuracy of Time-Accurate Turbulent Navier-Stokes Computations," *Computers and Fluids*, Vol. 25, No. 2, pp. 217-236, 1996.
- [14] McDevitt, J. B., Levy, L. L., and Deiwert, G. S., "Transonic Flow about a Thick Circular-Arc Airfoil," *AIAA Journal*, Vol. 14, No. 5, May 1976, pp. 606-613.
- [15] Piziali, R. A., "2-D and 3-D Oscillating Wing Aerodynamics for a Range of Angles of Attack Including Stall," NASA TM 4632, Sep. 1994.

## Figures

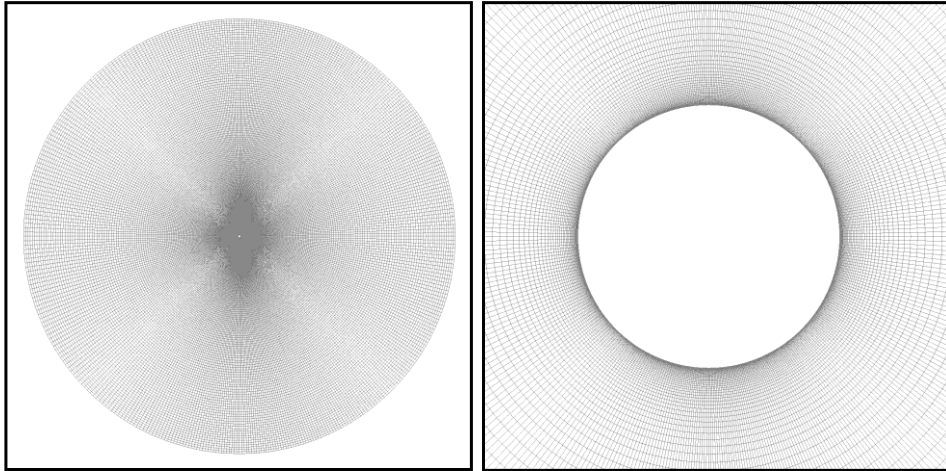


Figure 1. Structured grid of the circular cylinder used for the Cobalt and Beggar calculations

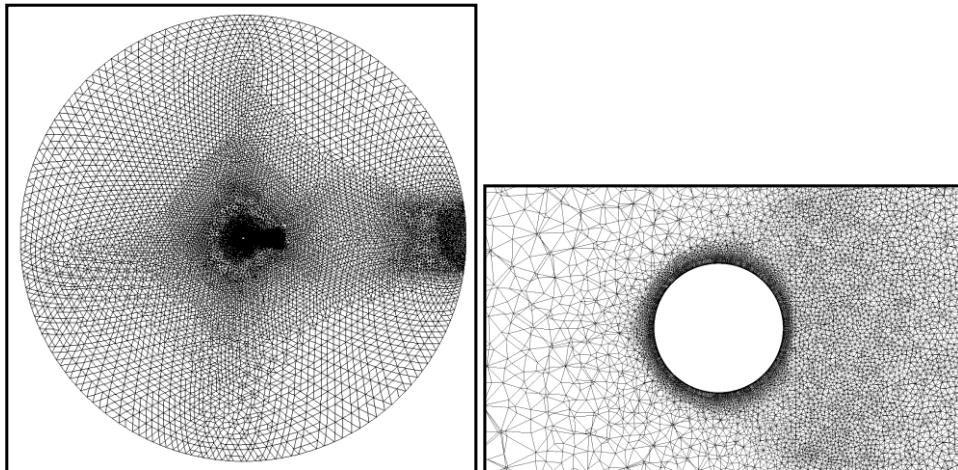


Figure 2. Unstructured grid of the circular cylinder used for the USM3D and FUN3D calculations.

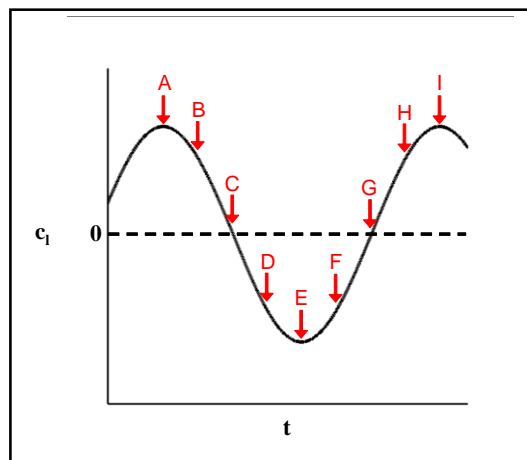


Figure 3. Lift coefficient as a function of time for the laminar circular cylinder at Mach 0.2,  $Re_c = 150$ ,  $\alpha = 0^\circ$  for the Cobalt flow solver.

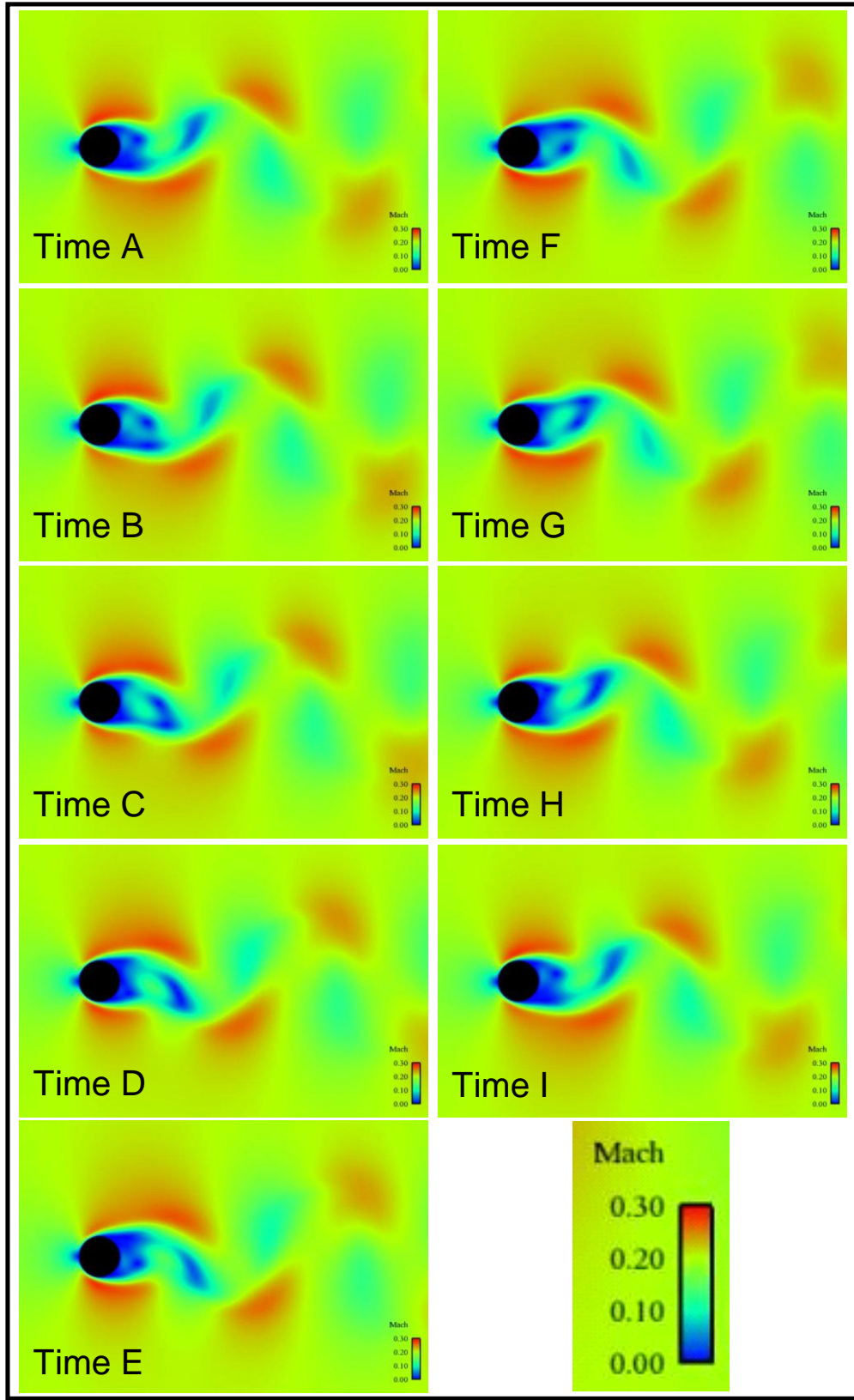


Figure 4. Mach number contours as a function of time for the laminar circular cylinder at Mach 0.2,  $Re_c = 150$ ,  $\alpha = 0^\circ$  for the Cobalt flow solver.

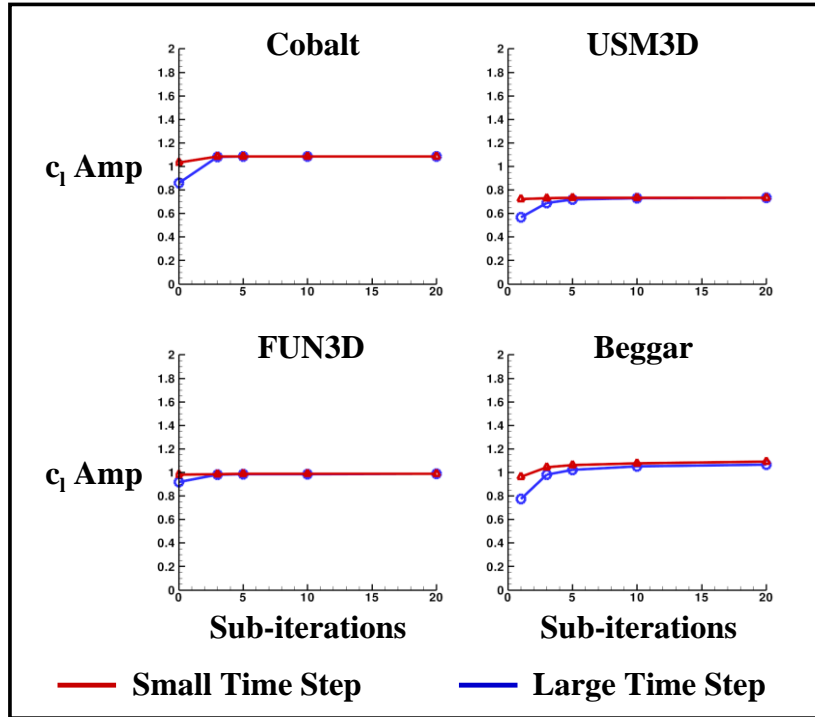


Figure 5. Amplitude of lift coefficient versus number of subiterations for the circular cylinder validation case.

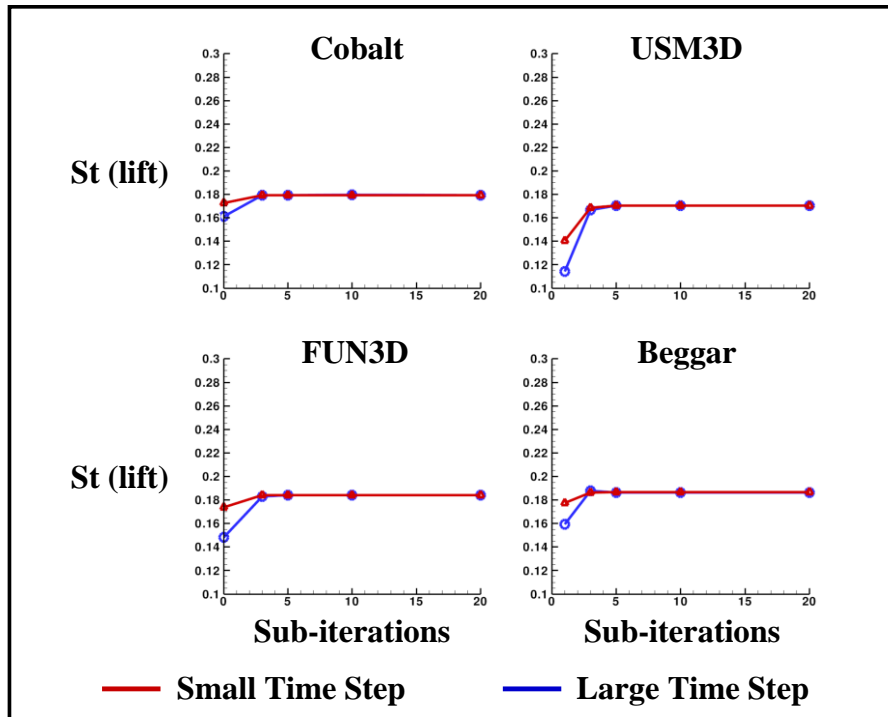


Figure 6. Lift Strouhal number versus number of subiterations for the circular cylinder validation case.

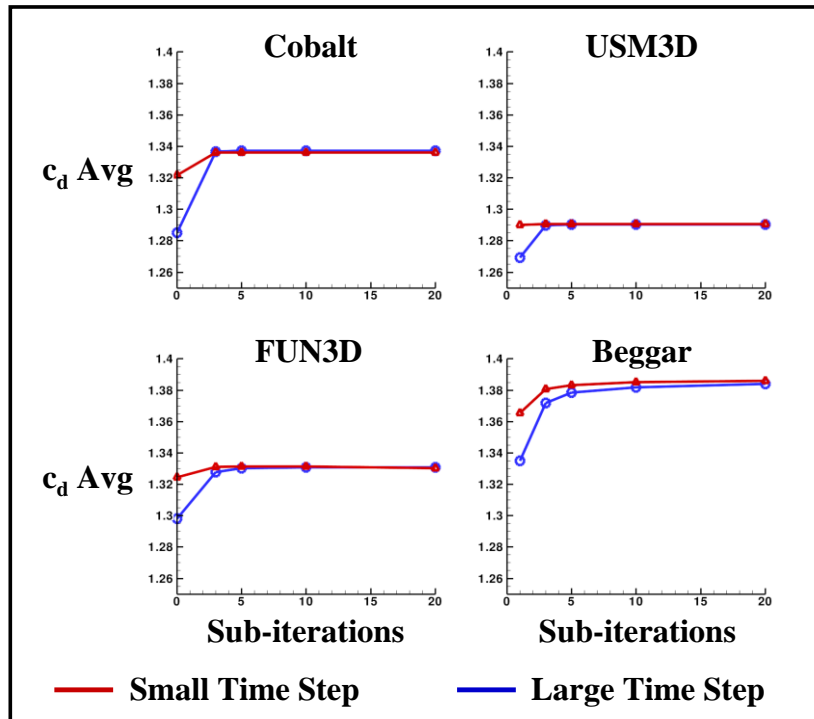


Figure 7. Average drag coefficient versus number of subiterations for the circular cylinder validation case.

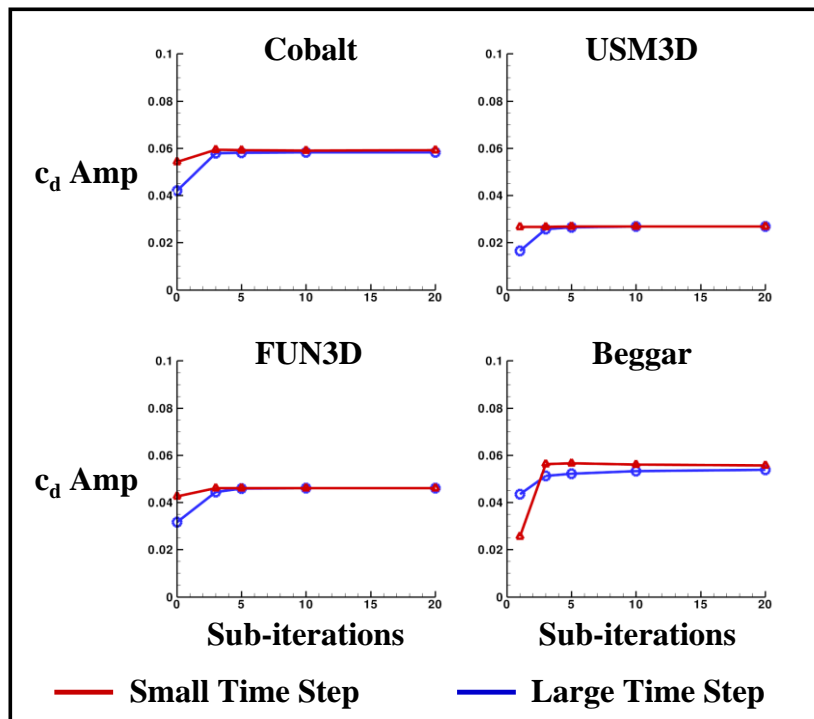


Figure 8. Amplitude of drag coefficient versus number of subiterations for the circular cylinder validation case.

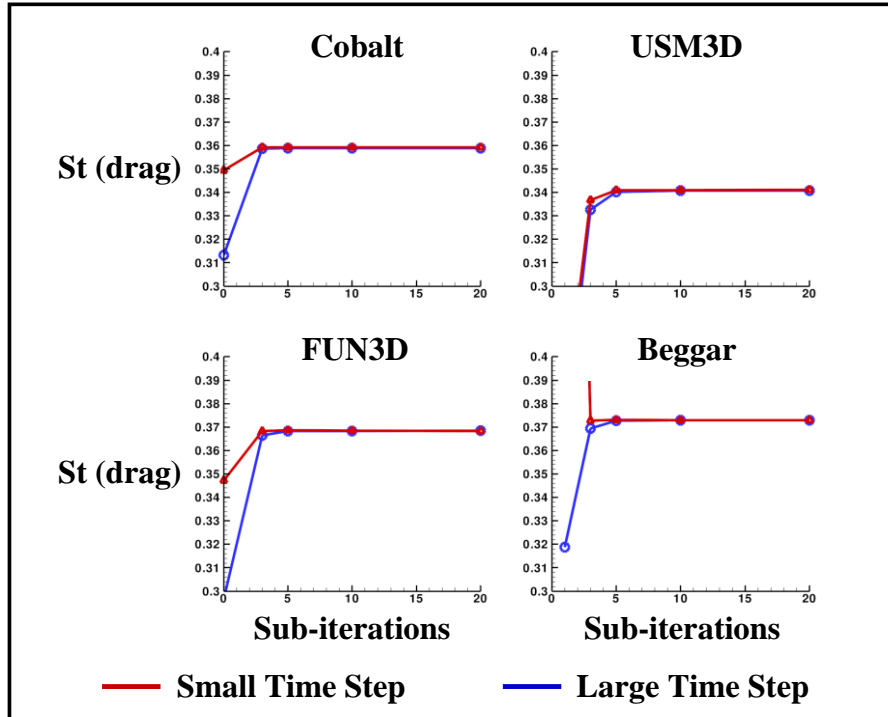


Figure 9. Drag Strouhal number versus number of subiterations for the circular cylinder validation case.

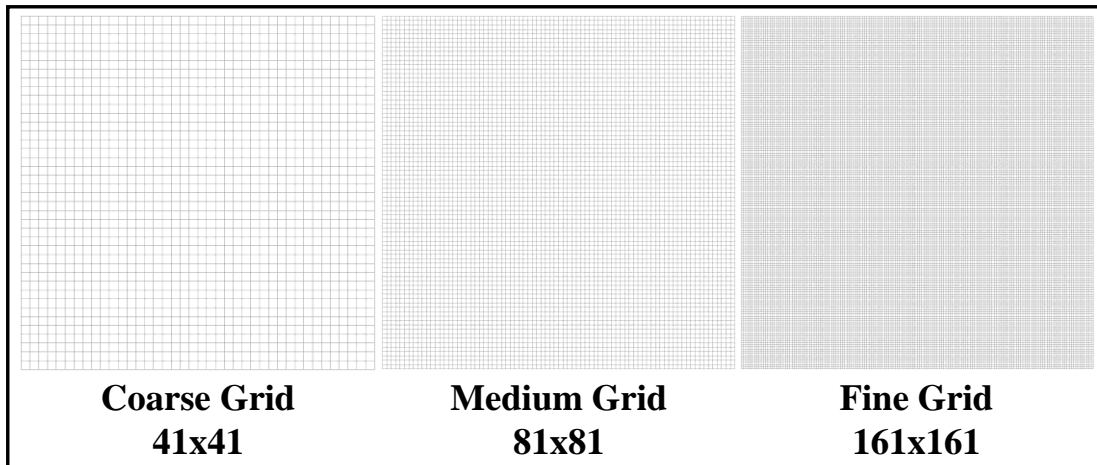


Figure 10. Coarse, medium and fine structured grids used for the Cobalt convecting vortex calculations.

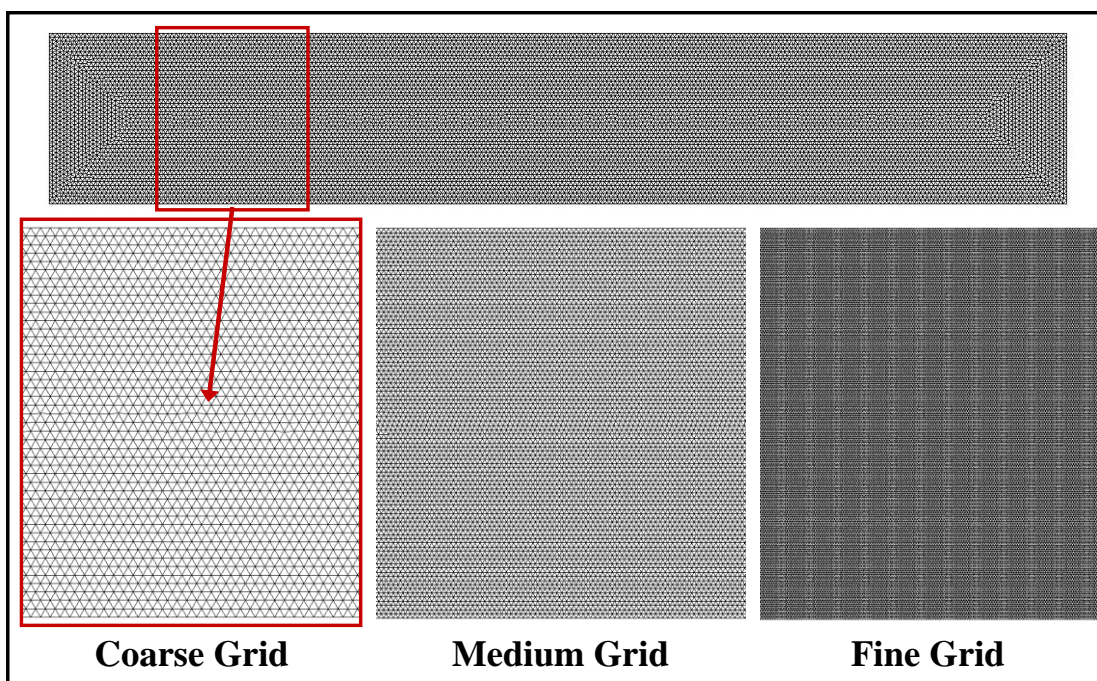


Figure 11. Coarse, medium and fine unstructured grids used for the USM3D and FUN3D convecting vortex calculations.

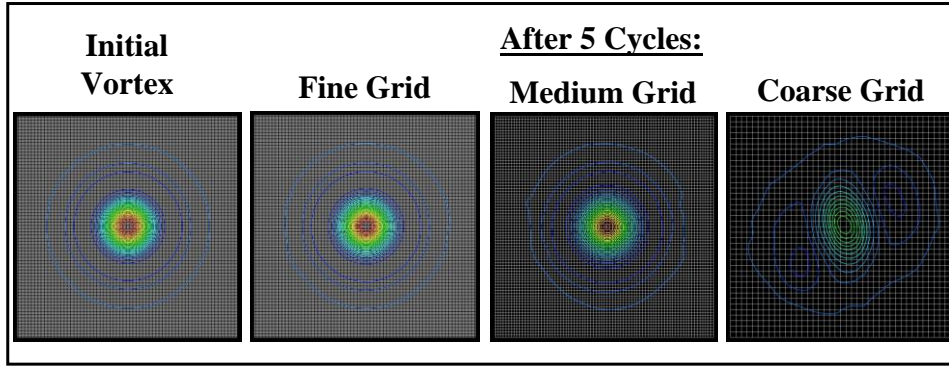


Figure 12. Results for Cobalt for the inviscid convecting vortex.

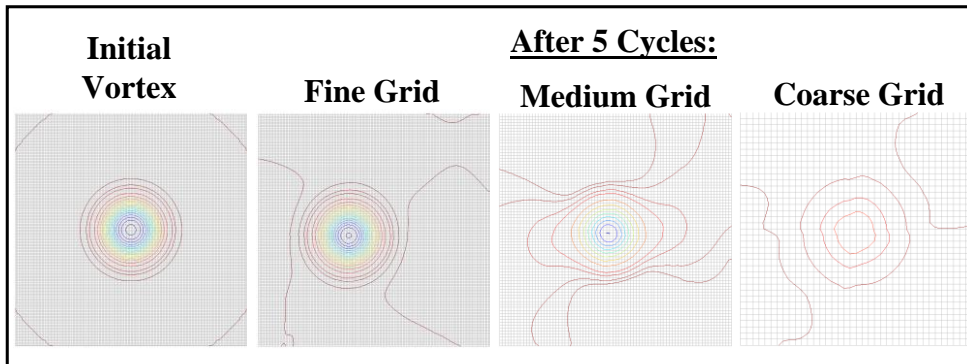


Figure 13. Results for Beggar for the inviscid convecting vortex.

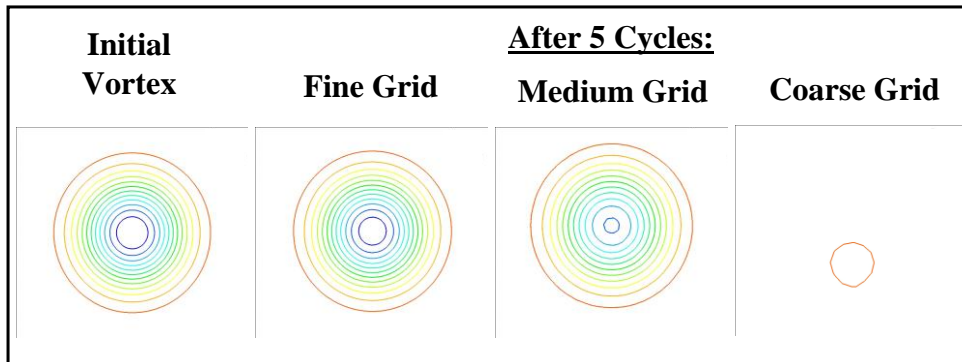


Figure 14. Results for FUN3D for the inviscid convecting vortex.

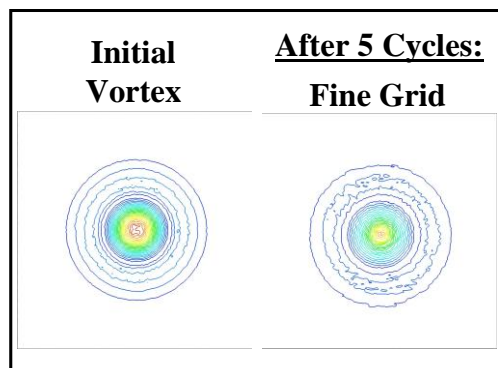


Figure 15. Results for USM3D for the inviscid convecting vortex.

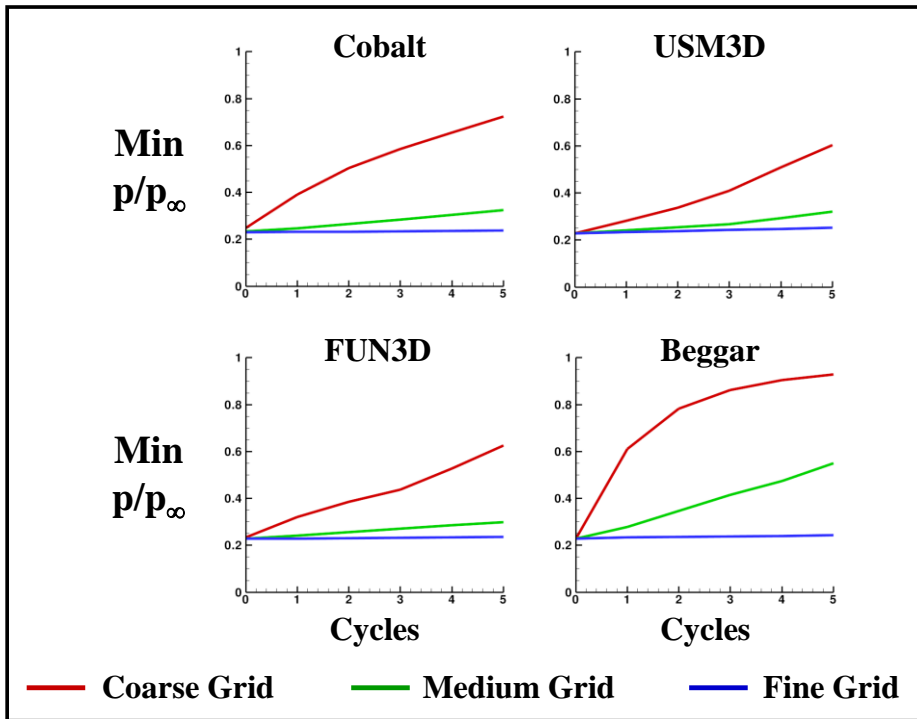


Figure 16. Minimum pressure versus cycles for the inviscid convecting vortex.

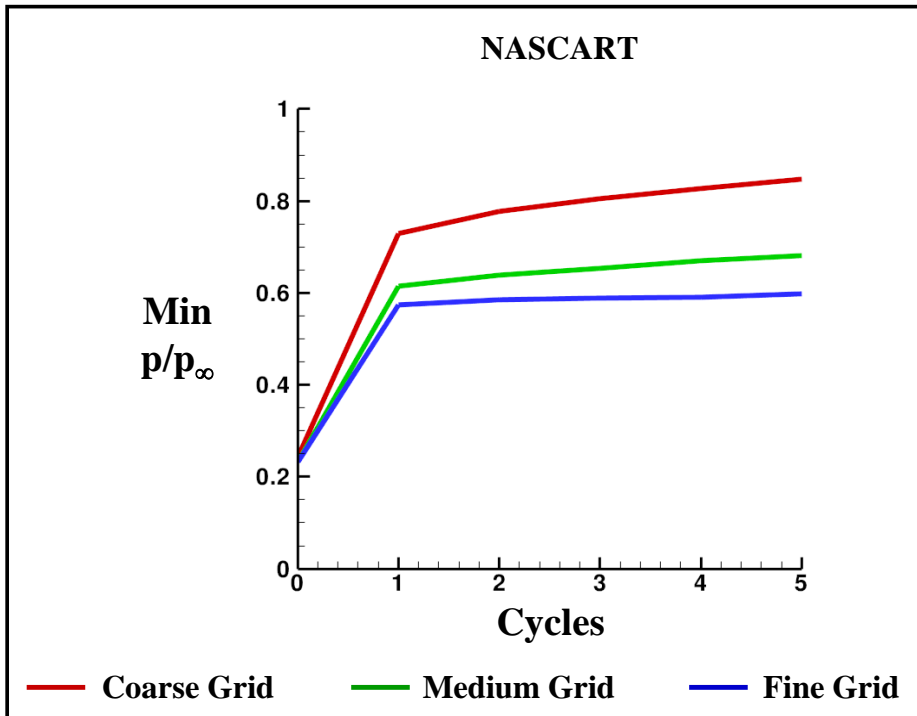


Figure 17. Minimum pressure versus cycles for the inviscid convecting vortex for NASCART.

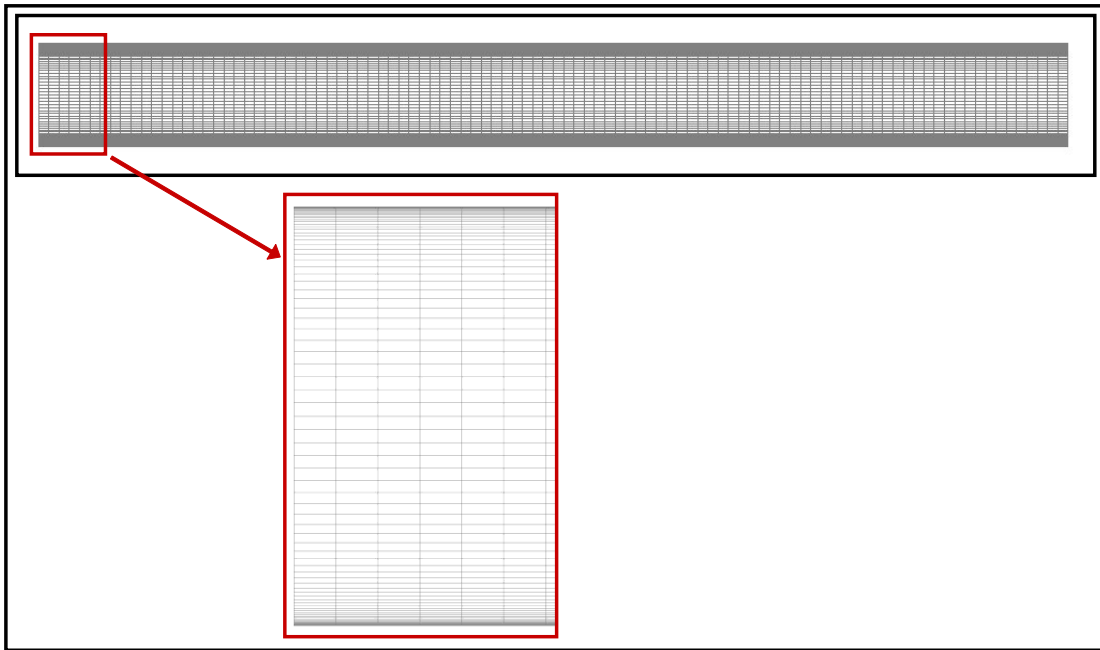


Figure 18. Structured grid of the shock tube used for the Cobalt and Beggar calculations.

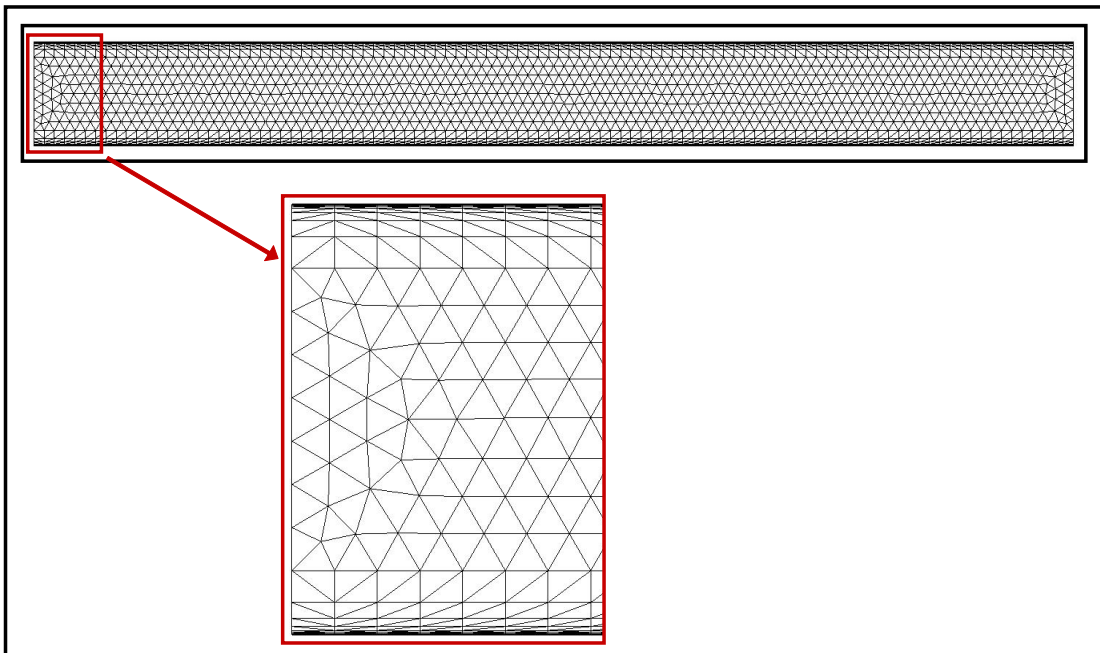


Figure 19. Unstructured grid of the shock tube used for the USM3D and FUN3D calculations.

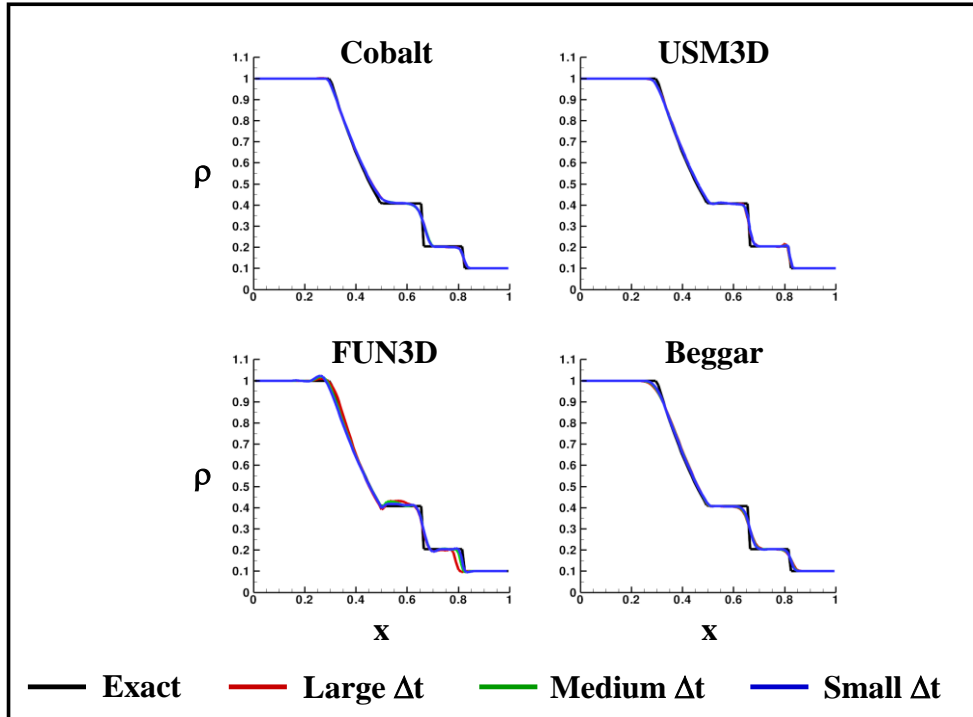


Figure 20. Density in the shock tube after a non-dimensional time of 0.2.

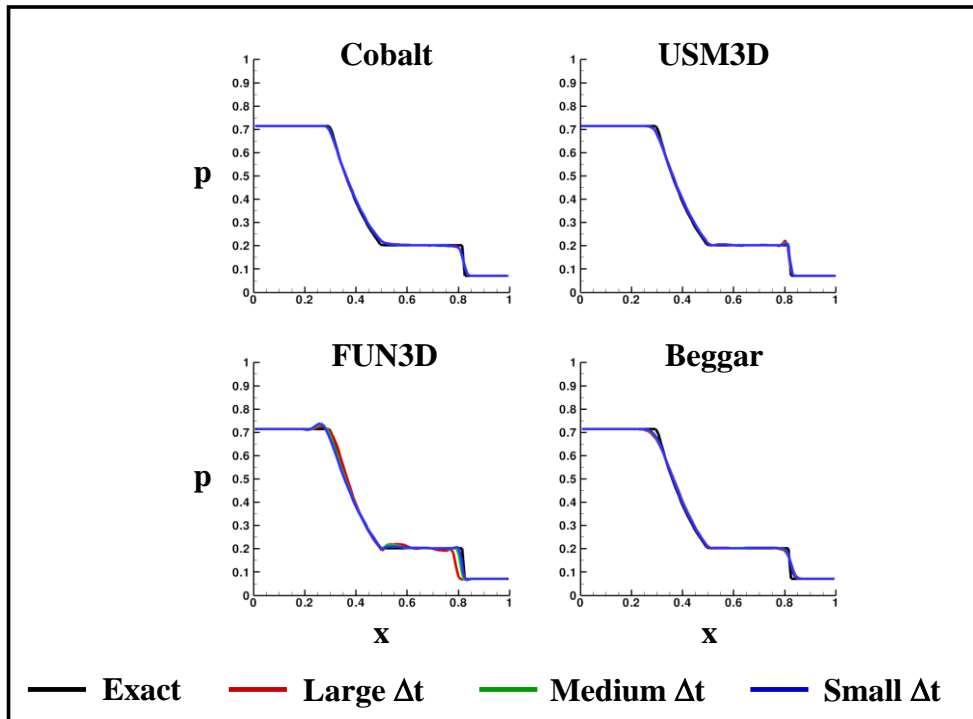


Figure 21. Pressure in the shock tube after a non-dimensional time of 0.2.

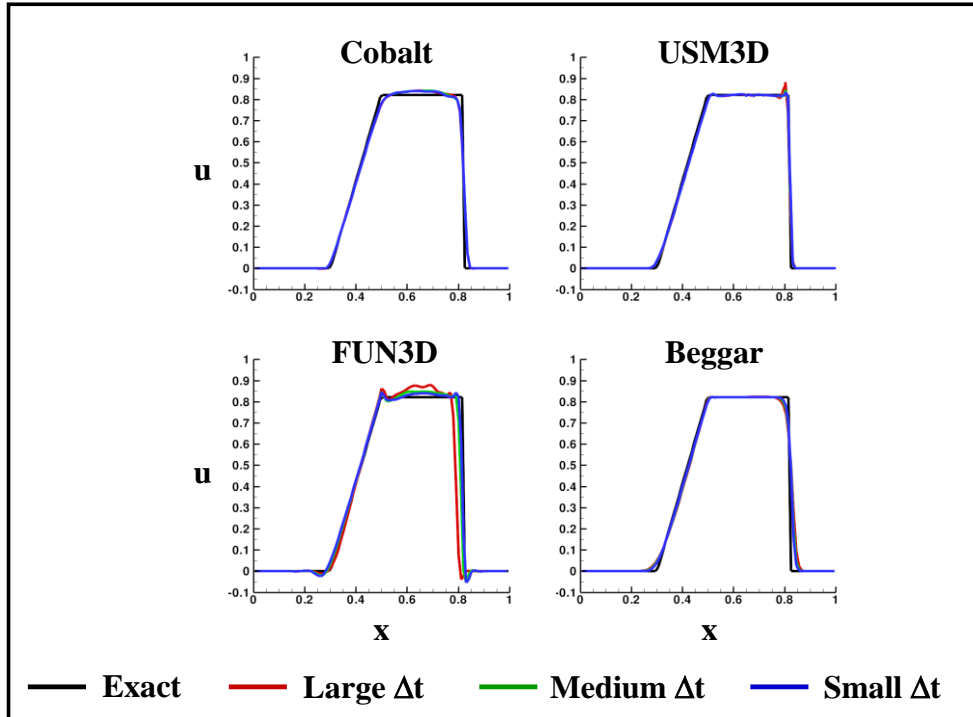


Figure 22. Velocity in the shock tube after a non-dimensional time of 0.2.

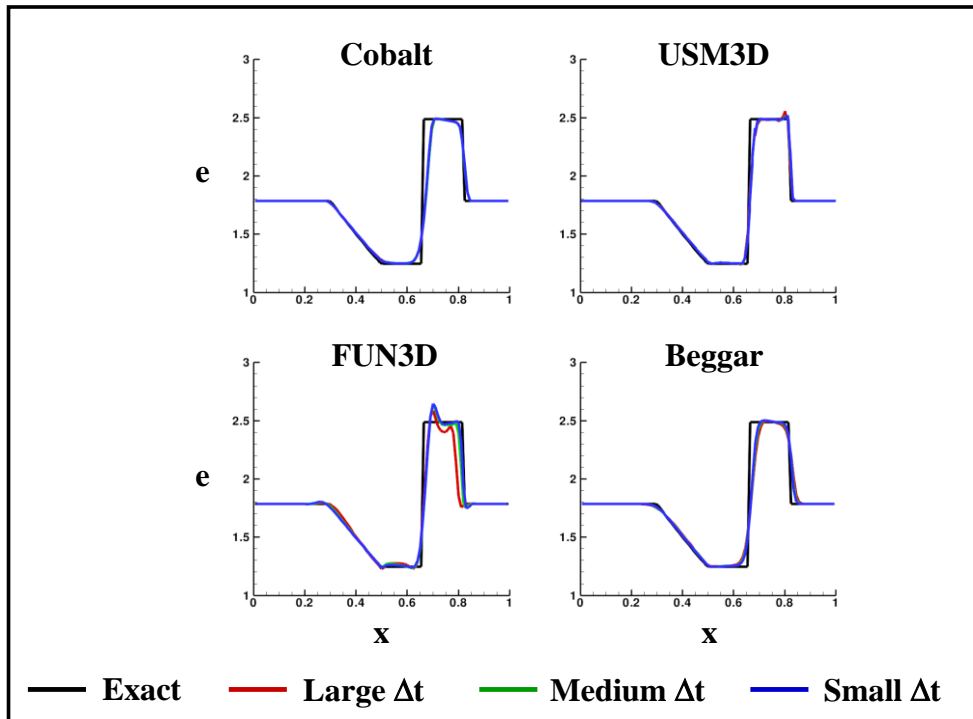


Figure 23. Energy in the shock tube after a non-dimensional time of 0.2.

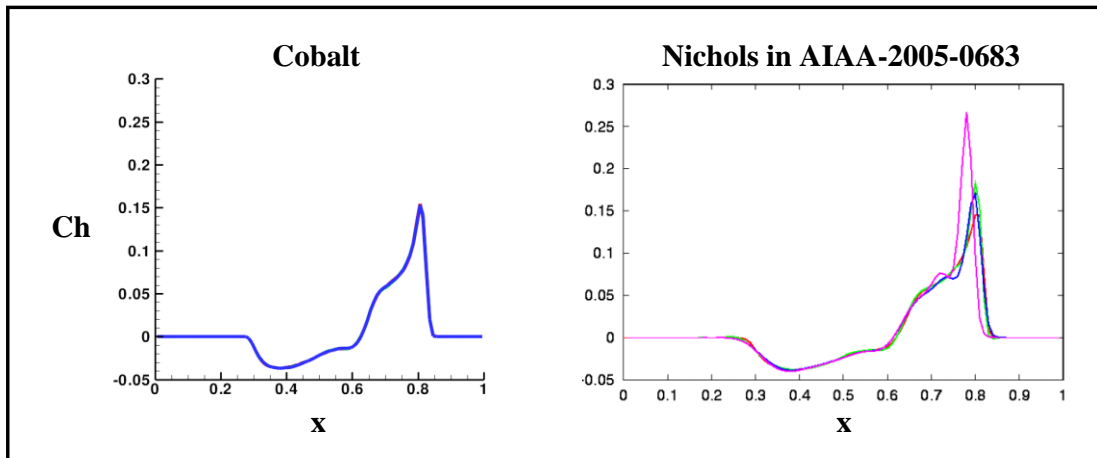


Figure 24. Wall heat coefficient in the shock tube after a non-dimensional time of 0.2.

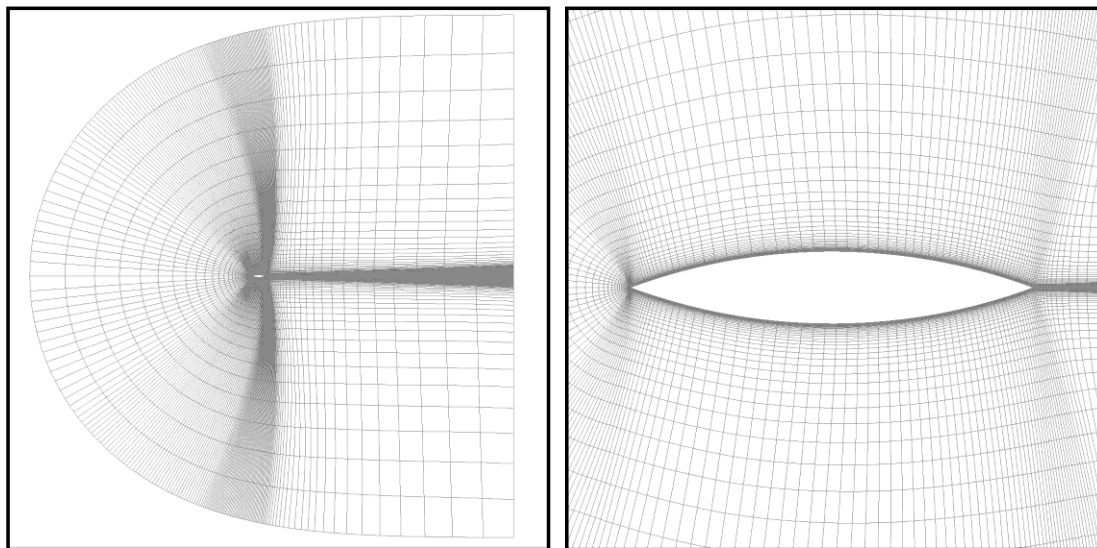


Figure 25. Structured grid of the 18%-thick circular-arc airfoil used for the Cobalt calculations.

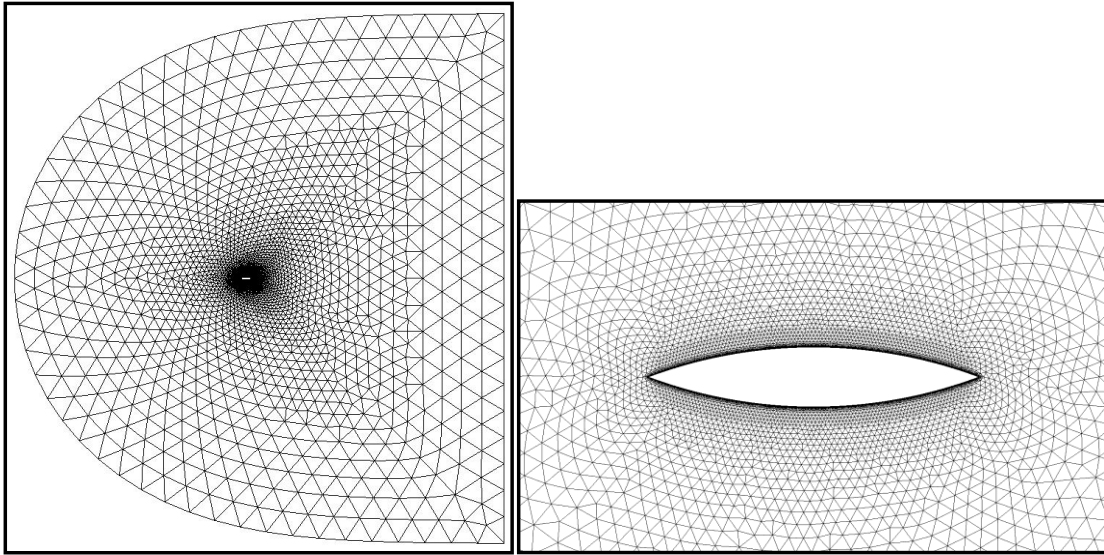


Figure 26. Unstructured grid of the 18%-thick circular-arc airfoil used for the USM3D and FUN3D calculations.

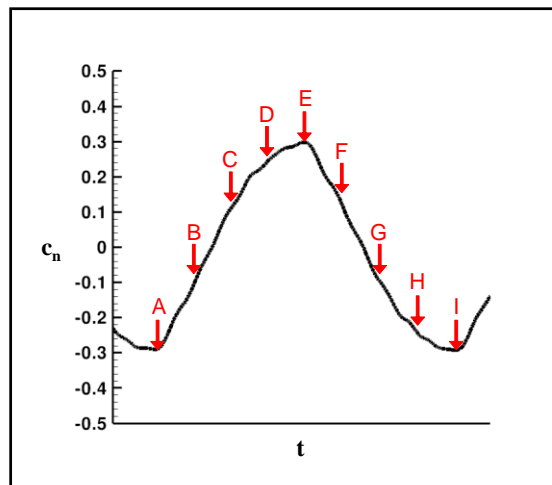


Figure 27. Normal force coefficient as a function of time for the 18%-thick circular-arc airfoil at Mach 0.76,  $Re_c = 12$  million,  $\alpha = 0^\circ$  for the Cobalt flow solver and the SST turbulence model.

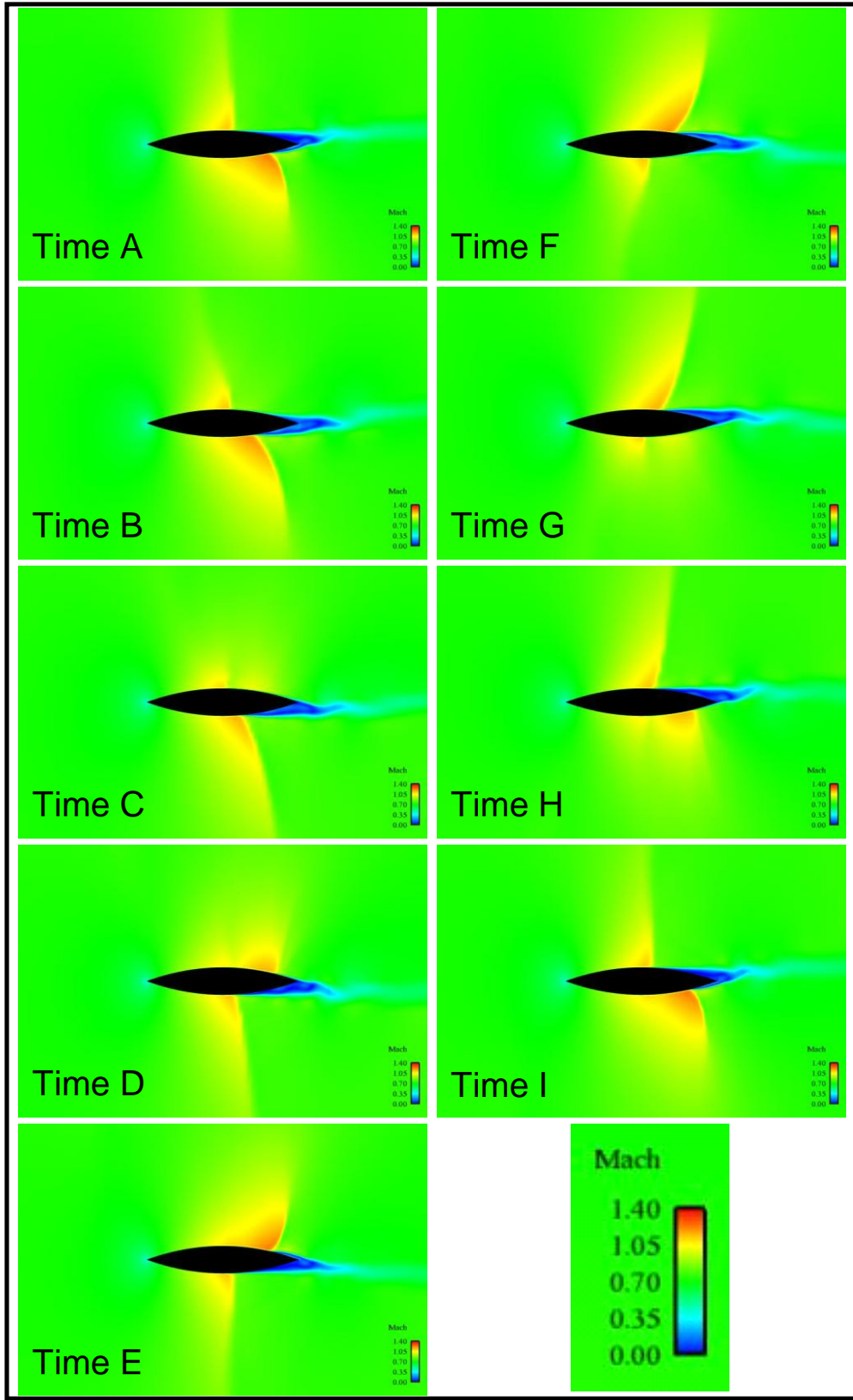


Figure 28. Mach number contours as a function of time for the 18%-thick circular-arc airfoil at Mach 0.76,  $Re_c = 12$  million,  $\alpha = 0^\circ$  with the Cobalt flow solver and the SST turbulence model.

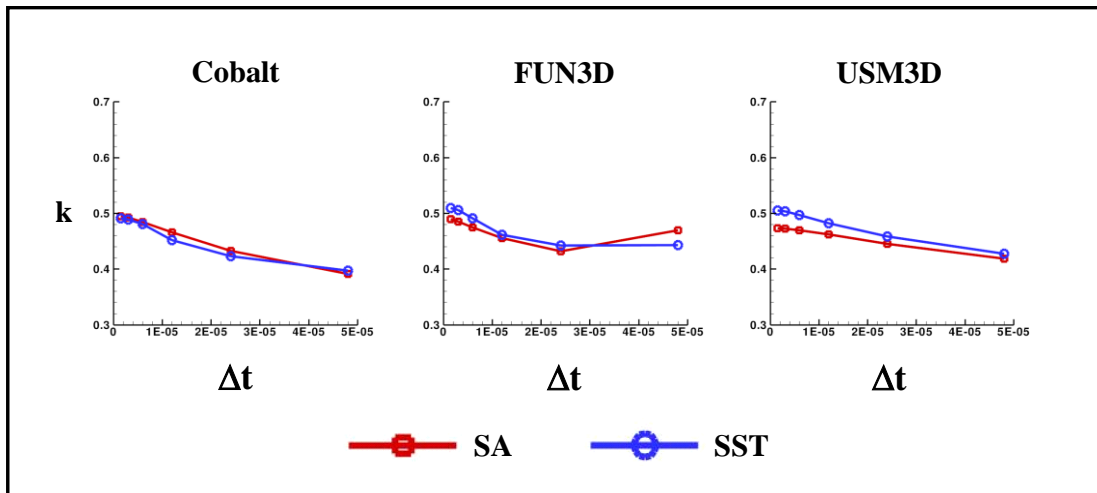


Figure 29. Reduced frequency versus time step for the 18%-thick circular-arc airfoil at Mach 0.76,  $Re_c = 12$  million,  $\alpha = 0^\circ$ .

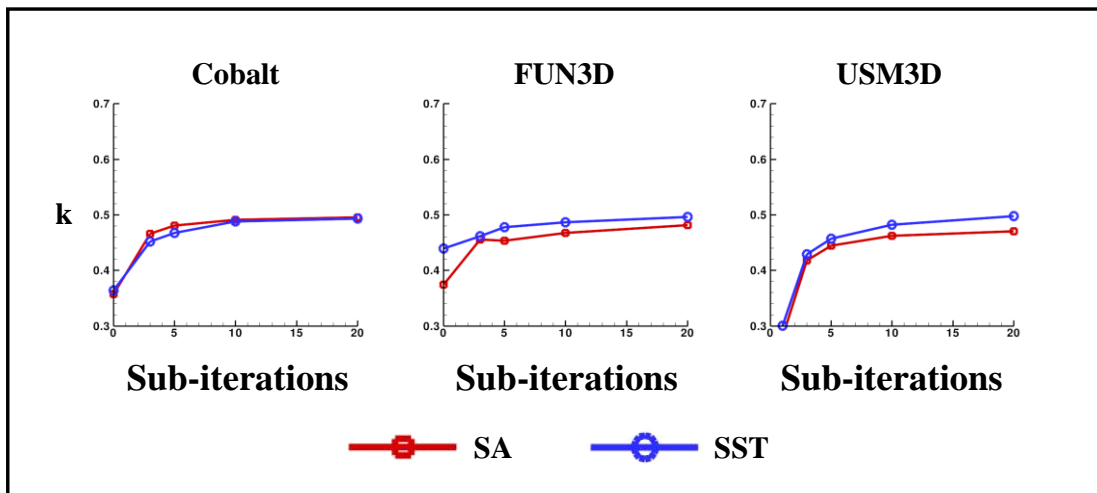


Figure 30. Reduced frequency versus subiterations for the 18%-thick circular-arc airfoil at Mach 0.76,  $Re_c = 12$  million,  $\alpha = 0^\circ$ .

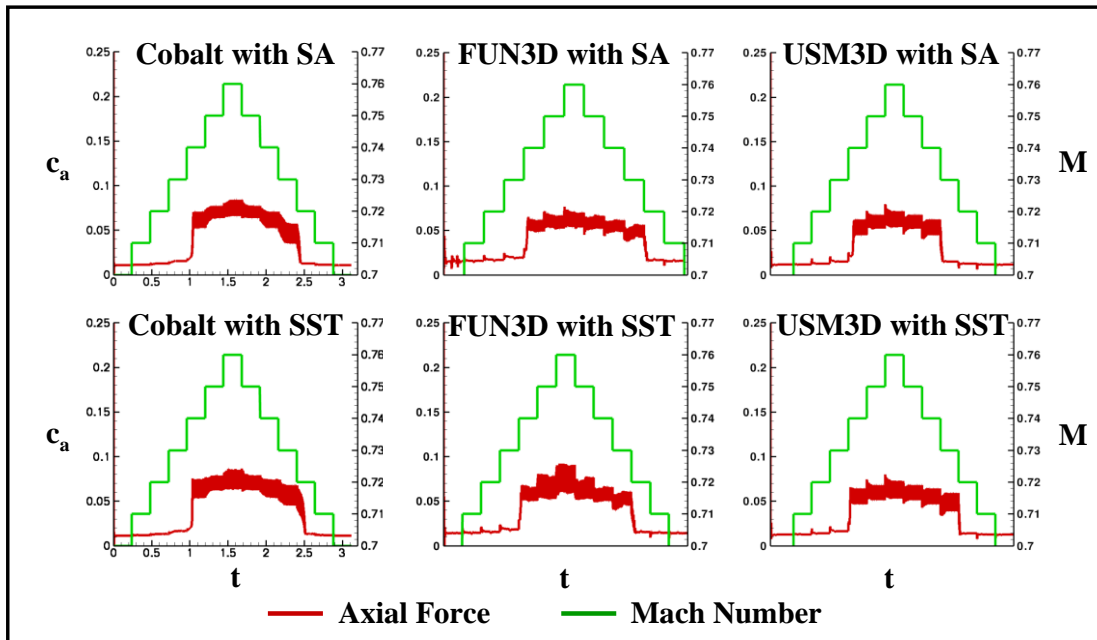


Figure 31. Axial-force coefficient versus time and Mach number for the 18%-thick circular-arc airfoil at  $\alpha = 0^\circ$ .

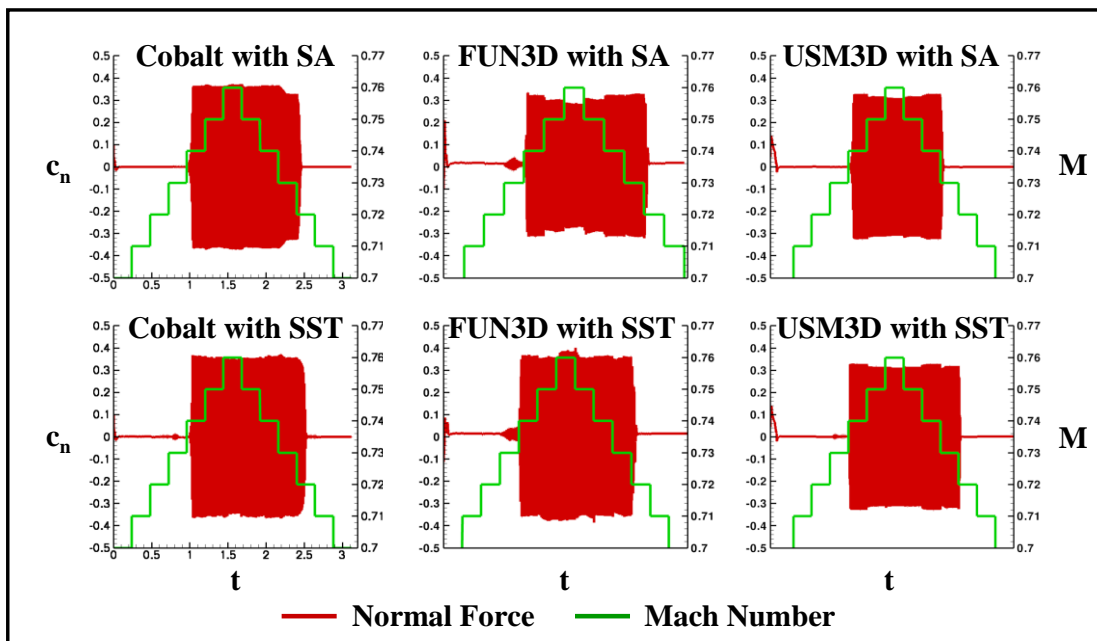


Figure 32. Normal-force coefficient versus time and Mach number for the 18%-thick circular-arc airfoil at  $\alpha = 0^\circ$ .

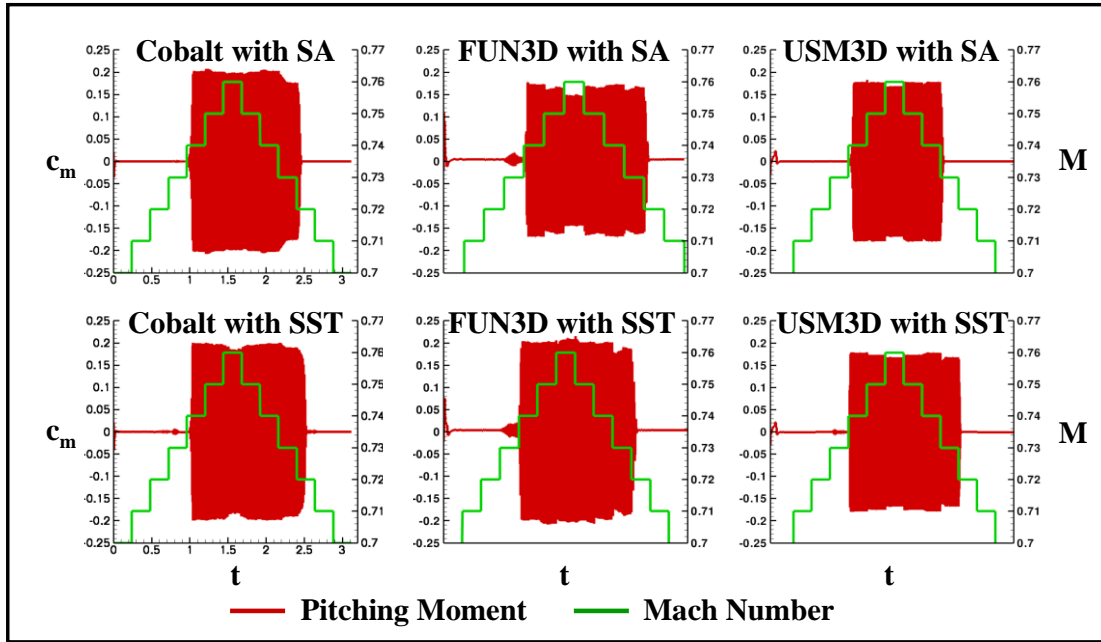


Figure 33. Pitching-moment coefficient versus time and Mach number for the 18%-thick circular-arc airfoil at  $\alpha = 0^\circ$ .

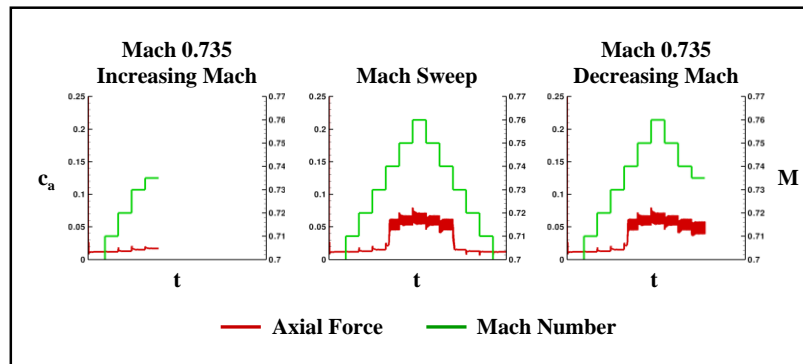


Figure 34. Axial-force coefficient versus time and Mach number for the 18%-thick circular-arc airfoil for USM3D with the SA turbulence model at  $\alpha = 0^\circ$ .

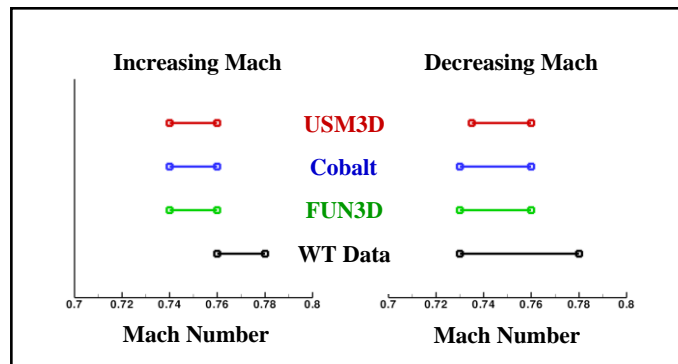
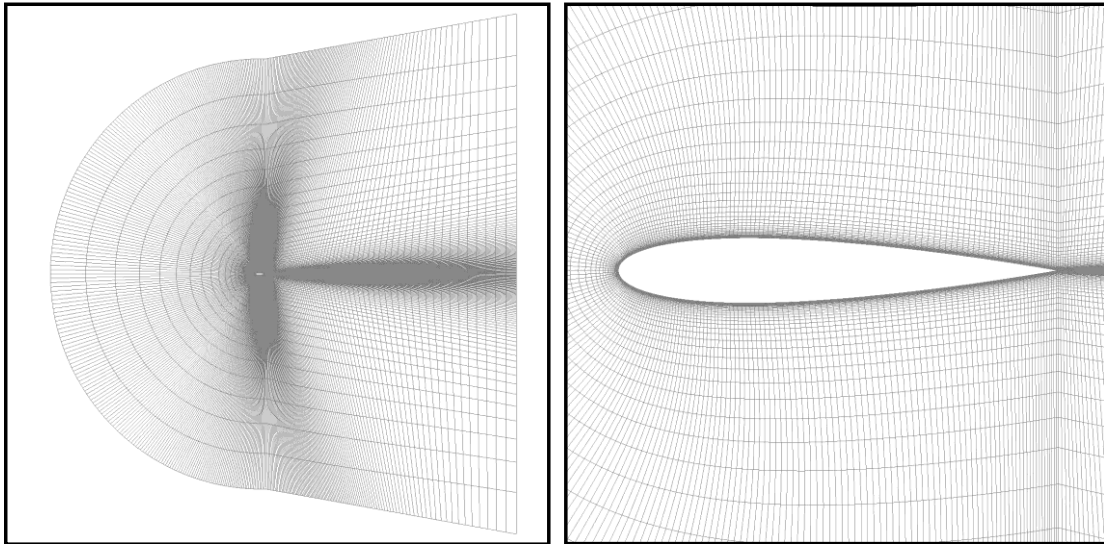
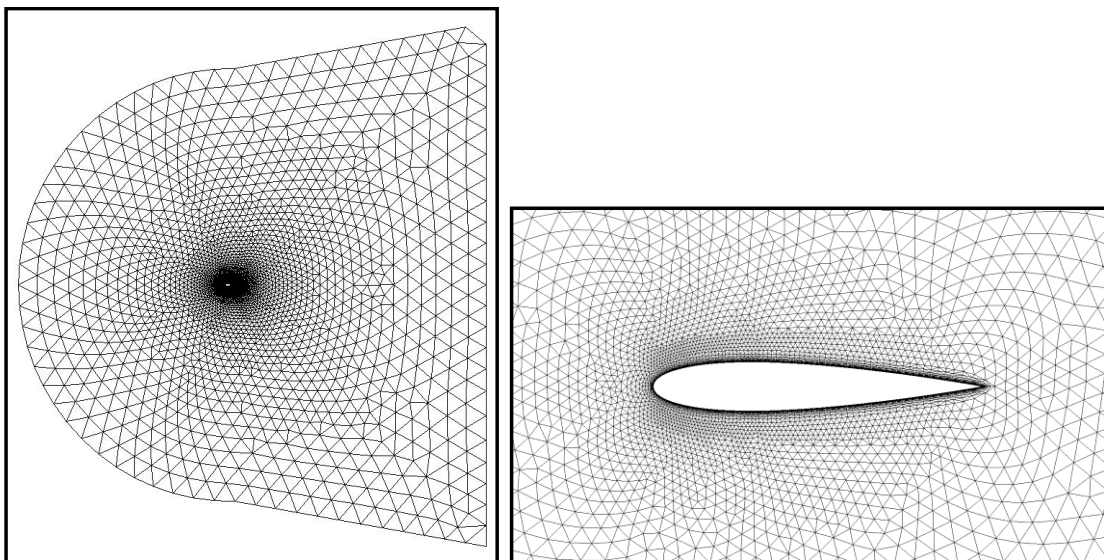


Figure 35. Regions of unsteady flow predicted by wind-tunnel experiment and the Cobalt, FUN3D, USM3D flow solvers for the 18%-thick circular-arc airfoil at  $\alpha = 0^\circ$ .



**Figure 36.** Structured grid of the NACA 0015 pitching airfoil that was used for the Cobalt calculations.



**Figure 37.** Unstructured grid of the NACA 0015 pitching airfoil that was used for the USM3D and FUN3D calculations.

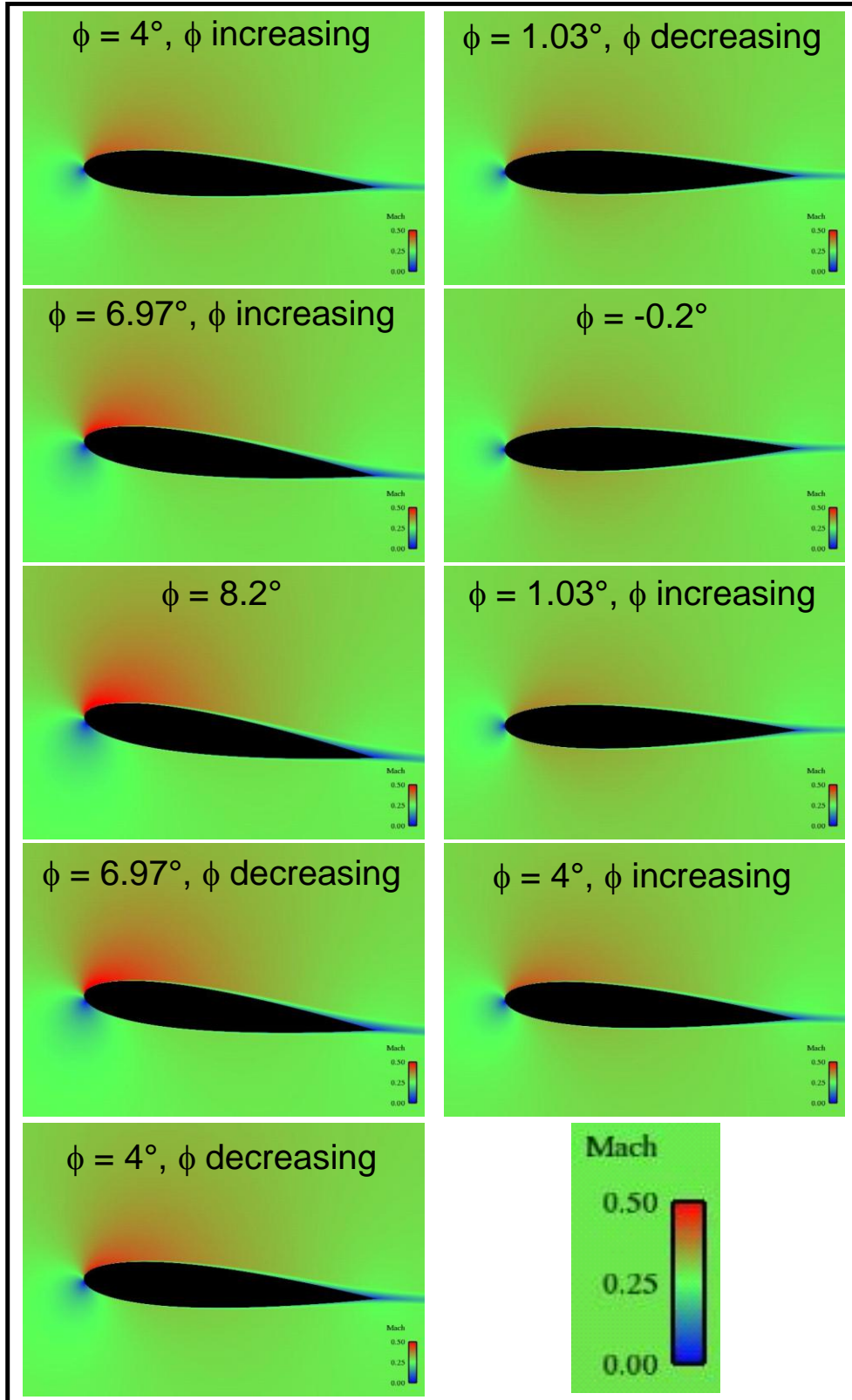


Figure 38. Mach number contours as a function of pitch angle for the NACA 0015 pitching airfoil at Mach 0.29,  $Re_c = 1.95$  million with the Cobalt flow solver and the SST turbulence model.

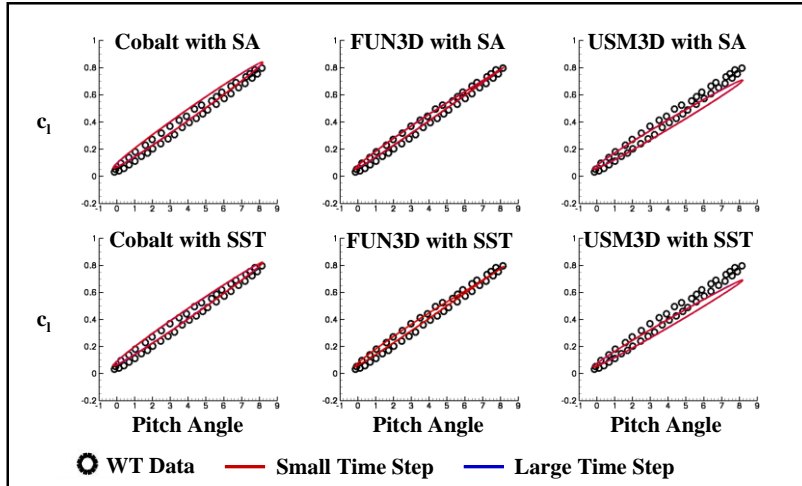


Figure 39. Lift coefficient as a function of pitch angle for the NACA 0015 pitching airfoil.

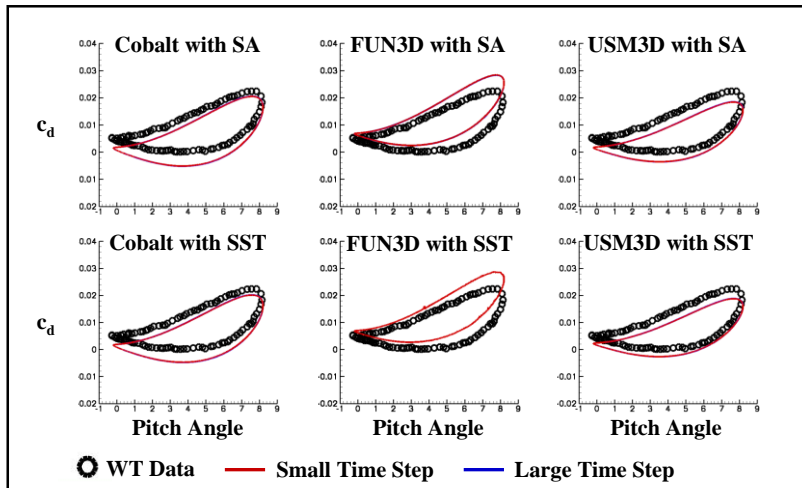


Figure 40. Drag coefficient as a function of pitch angle for the NACA 0015 pitching airfoil.

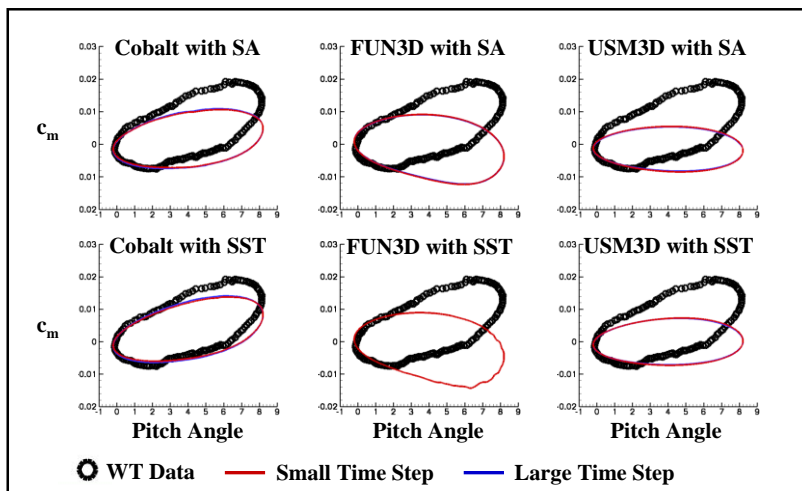


Figure 41. Pitching-moment coefficient as a function of pitch angle for the NACA 0015 pitching airfoil.